MOX-Report No. 29/2023

Design of innovative self-expandable femoral stents using inverse homogenization topology optimization

Carbonaro, D.; Mezzadri, F.; Ferro, N.; De Nisco, G.; Audenino, A.L.; Gallo, D.; Chiastra, C.; Morbiducci, U.; Perotto, S.

MOX, Dipartimento di Matematica
Politecnico di Milano, Via Bonardi 9 - 20133 Milano (Italy)

mox-dmat@polimi.it https://mox.polimi.it

Design of innovative self-expandable femoral stents using inverse homogenization topology optimization

Dario Carbonaro[1], Francesco Mezzadri[2], Nicola Ferro[3], Giuseppe De Nisco[1], Alberto Luigi Audenino[1], Diego Gallo[1], Claudio Chiastra[1], Umberto Morbiducci[1], Simona Perotto[3]

March 23, 2023

[1] PoliTo^{BIO}Med Lab, Department of Mechanical and Aerospace Engineering
Politecnico di Torino
Viale Duca degli Abruzzi, 24, Torino, Italy

[2] Department of Engineering Enzo Ferrari
University of Modena and Reggio Emilia
Via P. Vivarelli, 10/1, Modena, Italy

[3] MOX – Dipartimento di Matematica
Politecnico di Milano
Piazza L. da Vinci, 32, I-20133 Milano, Italy

Abstract

In this study, we propose a novel computational framework for designing innovative self-expandable femoral stents. First, a two-dimensional stent unit cell is designed by inverse homogenization topology optimization. In particular, the unit cell is optimized in terms of contact area with the target of matching prescribed mechanical properties. The topology optimization is enriched by an anisotropic mesh adaptation strategy, enabling a time- and cost-effective procedure that promotes original layouts. Successively, the optimized stent unit cell is periodically repeated on a hollow cylindrical surface to construct the corresponding three-dimensional device. Finally, structural mechanics and computational fluid dynamics simulations are carried out to verify the performance of the newly-designed stent. The proposed workflow is being tested through the design of five proof-of-concept stents. These devices are compared through specific performance evaluations, which include the assessments of the minimum requirement for usability, namely the ability to be crimped into a catheter, and the quantification of the radial force, the foreshortening, the structural integrity and the induced blood flow disturbances.

Keywords: Peripheral artery disease, Nitinol stent, topology optimization, homogenization, anisotropic adapted mesh, computational fluid dynamics

1 Introduction

Vascular stents are minimally invasive mechanical devices designed as cylinder-like hollow structures, obtained, in general, by the periodic repetition of a unit cell. Stent devices are deployed inside diseased blood vessels for providing mural support and preventing vessel obstruction after intervention. Available with different shapes, sizes and materials, depending on the treated pathology and implantation site, most of the stents are metallic and have a narrow profile in a crimped (i.e., radially compressed) state to easily pass and be placed inside the vessels [1, 2, 3, 4]. Vascular stents are commonly divided into two major categories depending upon the deployment procedure [5]: balloon-expandable stents, usually made of stainless-steel, cobalt or platinum chromium alloy, which are manufactured in a crimped state and are plastically expanded to the vessel wall by balloon inflation; self-expandable stents, typically made of super-elastic Nickel-Titanium (NiTi), which are manufactured slightly oversized above the vessel diameter and elastically resume their initial shape after being crimped and released from the catheter, without the need for balloon inflation [1, 6].

Whether it is a balloon- or a self-expandable device, stents may lead to well-established clinical issues, such as in-stent restenosis (ISR) (i.e., gradual vessel lumen re-narrowing caused by abnormal neointimal proliferation) and stent thrombosis (i.e., sudden occlusion of the vessel due to the formation of a blood clot), which represent two of the major complications still limiting the safety and success of stenting [7, 8, 9]. It has been verified that the geometric features of the stent unit cells may have a direct impact on the occurrence of ISR and stent thrombosis and, more in general, on the mechanical performance of the devices as well as on the clinical outcome of the treatment [3, 4, 8, 10, 11, 12, 13].

Over the last decades, significant research efforts have been conducted to improve the design of the stent unit cells for the obtainment of an adequate response of the device. Within this context, computational methods have been used as an efficient tool to virtually characterize and optimize the stent design, with great advantages in terms of associated costs. In recent years, *in silico* models have gained increasing momentum by the medical device industry, and structural mechanics simulations are commonly adopted to support the design process of stents, especially in the initial proof-of-concept stage [14, 15]. For instance, several computational frameworks, merging geometric- with physics-based features, have been developed to optimize the mechanical performance of stents with the final goal of improving the effectiveness of the endovascular treatment [16, 17, 18, 19, 20, 21, 22].

Among the optimization strategies available for supporting the design of vascular stents, topology optimization (TO) represents an attractive procedure for the systematic design of new layouts of the devices. The idea is to optimize the topology of the stent in order to match specific design

requirements [23]. Few contributions are available in the literature where a TO-based strategy is applied to vascular stent design. As possible examples, TO-based approaches have been applied to: a commercially available drug-eluting stent, aiming at increasing the stent strut stiffness while retaining the drug holding capacity [24]; optimize the stent material layout, tailoring the structure to achieve a bi-stable snap-through behavior [25]; investigate the material distribution of coronary artery auxetic stents, improving both the structural and hemodynamic properties of the device [26, 27].

In this work, we propose a computational framework based on TO for the design of innovative self-expandable femoral stents to be deployed inside diseased femoropopliteal arteries. This task is particularly challenging due to the severe deformations that femoropopliteal arteries undergo during lower limb movements [28, 29], which in turn impose complex loading conditions to the implanted devices, leading to high failure rates [7]. The computational framework here presented is inspired by inverse homogenization, namely a consolidated technique for the optimal design of microscopic unit cells that confer desired properties to a lattice material at the macroscale [23]. Thus, since a stent can be conceived as the repetition of a unit cell onto a cylindrical surface, we aim to design from scratch new stent unit cells to ideally guarantee geometric, structural or hemodynamic properties to the whole device. With this aim, we resort to the microSIMPATY algorithm [30] which enhances a standard inverse homogenization topology optimization approach with a customized choice of the computational mesh in a finite element setting. In more detail, an anisotropic adapted mesh is adopted to make the design process time- and cost-effective through a fully automatic procedure. This phase constitutes the first step of a new design workflow that sequentially generates two-dimensional stent unit cells, periodically repeats the optimized cells on a hollow cylindrical surface for generating the three-dimensional stent design, and, finally, verifies the response of the device in terms of structural mechanics and computational fluid dynamics criteria.

The paper is organized as follows. Section 2 represents the modeling and methodological core of the manuscript, by setting the workflow yielding the new stent designs. In particular, after setting the stent design requirement and the assessment criteria under consideration in this work, in Section 2.1 we formalize the inverse homogenization TO procedure, with an example of an innovative 2D cell. Section 2.2 deals with the generation of a 3D stent, starting from the optimized unit layout. Sections 2.3 and 2.4 describe the structural mechanics and CFD analysis performed on the new stent designs. Section 3 is devoted to the numerical assessment of the whole pipeline on five proof-of-concept cell layouts. Section 4 discusses the obtained results, the limitations of the proposed methodology and some hints on possible future perspectives. Finally, Section 5 gathers concluding remarks.

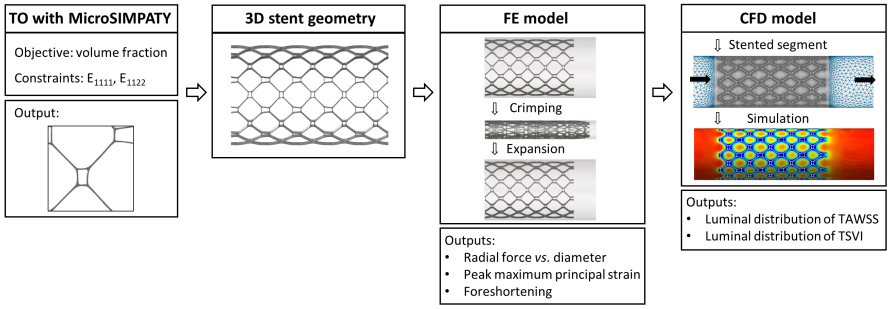

Figure 1: Main steps of the workflow for the design and verification of new self-expandable femoral artery stents.

2 Methods

The proposed procedure for the design of self-expandable femoral artery stents consists of the steps in Fig. 1, namely: *i*) inverse topology optimization (TO) to generate 2D designs of stent unit cells meeting specific requirements (see Section 2.1); *ii*) use of the identified 2D unit cells as the basis for generating 3D stent models (see Section 2.2); *iii*) finite element (FE)-based simulations of the complete crimping cycle of the 3D stent models generated in *ii)*, in order to evaluate the nonlinear structural behavior (see Section 2.3); *iv*) computational fluid dynamics (CFD) simulations on the generated 3D stent models in idealized vessels to assess the hemodynamic impact (see Section 2.4). The rationale behind the workflow in Fig. 1 is the ambitious goal of proposing innovative stents, which match prescribed structural/fluid dynamics demands and comply with standard regulations for vascular clinical practices. Indeed, femoral artery stents are expected to ensure specific geometric, structural and hemodynamic performances minimizing the risks associated with the implantation.

In detail, in the design phase *i)* of the workflow we minimize the contact area between the stent and the luminal surface of the vessel, which, in turn, reduces the risks associated with tissue ingrowth, in-stent restenosis (ISR) and thrombosis [31, 32]. A posteriori, to assess the biomechanical behaviour of the femoral stent, in the validation phases *iii)* and *iv)*, we focus on:

- the radial force applied by the implanted stent to the vessel wall, that has to be adequate for scaffolding the diseased artery, thus avoiding the damaging of the surrounding arterial wall tissue [3, 33, 34];
- the foreshortening of the stent, that enables a precise placement (i.e., covering the whole length of the lesion) once expanded in situ [3, 33, 34];
- the structural integrity of the stent, which is guaranteed by low (peak)

maximum principal strains on the stent when encased inside the delivery system [18];

- the blood flow disturbances induced by the struts of the implanted stent, which are expected to be minimal, in order to damp the risk factors promoting ISR or thrombosis [31].

2.1 The design of unit stent cells

The design of 2D stent unit cells – namely the first step of the workflow in Fig. 1 – has the principal goal to minimize the contact area of the stent, jointly with the enforcement of suitable constraints on the internal stress of the stent unit cells, under prescribed loading conditions. With this aim, we adopt the microSIMPATY algorithm [30], which allows designing from scratch unit cells targeting prescribed properties through a TO process. Physical background and technical details of microSIMPATY tool are provided in the two following sections and successively applied to a benchmark configuration in Section 2.1.3.

2.1.1 The physical background and the design strategy

MicroSIMPATY combines a standard topology optimization approach with the homogenization theory, and resorts to an anisotropic mesh adaptation procedure to increase the computational efficiency of the whole design algorithm. Hereafter, we formalize the reference physical framework, the selected topology optimization method, and the discretization scheme based on adapted meshes.

The homogenization theory The physical setting that we adopt to design stent unit cells is represented by the homogenized linear elasticity model [35, 36]. Homogenization is the standard mathematical process used to incorporate the information associated with the small scales (the stent unit cell, in the case under study) into a macroscopic problem (the whole stent). By resorting to an asymptotic expansion, it is customary to express the material properties by means of a single quantity, $E^H \in \mathbb{R}^{3\times3}$, which replaces the stiffness tensor $E \in \mathbb{R}^{3\times3}$ in the linear constitutive stress-strain relation $\boldsymbol{\sigma}(\boldsymbol{u}) = E\boldsymbol{\varepsilon}(\boldsymbol{u})$, with $\boldsymbol{u}$ the displacement,

$$\boldsymbol{\sigma}(\boldsymbol{u}) = \begin{pmatrix} \sigma_{11}(\boldsymbol{u}) \\ \sigma_{22}(\boldsymbol{u}) \\ \sigma_{12}(\boldsymbol{u}) \end{pmatrix}, \quad \boldsymbol{\varepsilon}(\boldsymbol{u}) = \begin{pmatrix} \varepsilon_{11}(\boldsymbol{u}) \\ \varepsilon_{22}(\boldsymbol{u}) \\ 2\varepsilon_{12}(\boldsymbol{u}) \end{pmatrix}, \quad E = \begin{pmatrix} E_{1111} & E_{1122} & E_{1112} \\ E_{2211} & E_{2222} & E_{2212} \\ E_{1211} & E_{1222} & E_{1212} \end{pmatrix}, \tag{1}$$

where $\boldsymbol{\varepsilon}$ denotes the strain tensor $\left(\nabla\boldsymbol{u} + \nabla\boldsymbol{u}^T\right)/2$ according to the Voigt notation [37]. Thus, we end up with the homogenized constitutive stress-strain relation $\boldsymbol{\sigma}^H(\boldsymbol{u}) = E^H\boldsymbol{\varepsilon}(\boldsymbol{u})$, where the stiffness tensor E^H can be

expressed componentwise by

$$E^H_{ijkl}(\boldsymbol{u}^{*,ij}, \boldsymbol{u}^{*,kl}) = \frac{1}{|\Omega|}\int_\Omega [\boldsymbol{\sigma}(\boldsymbol{u}^{0,ij}) - \boldsymbol{\sigma}(\boldsymbol{u}^{*,ij})] : [\boldsymbol{\varepsilon}(\boldsymbol{u}^{0,kl}) - \boldsymbol{\varepsilon}(\boldsymbol{u}^{*,kl})] d\Omega, \quad (2)$$

where $\Omega \subset \mathbb{R}^2$ denotes the unit cell of the stent, while $\boldsymbol{u}^{*,mn}$ are the fluctuations induced by the test displacement fields $\boldsymbol{u}^{0,mn}$, for $mn = ij, kl \in \mathcal{I} = \{11, 22, 12\}$, with $\boldsymbol{u}^{0,11} = (x_1, 0)^T$, $\boldsymbol{u}^{0,22} = (0, x_2)^T$, $\boldsymbol{u}^{0,12} = (x_2, 0)^T$. Fluctuations $\boldsymbol{u}^{*,mn}$ belong to a function space V to be properly selected and satisfy the equation

$$\int_\Omega \boldsymbol{\sigma}(\boldsymbol{u}^{*,mn}) : \boldsymbol{\varepsilon}(\boldsymbol{v}) d\Omega = \int_\Omega \boldsymbol{\sigma}(\boldsymbol{u}^{0,mn}) : \boldsymbol{\varepsilon}(\boldsymbol{v}) d\Omega \quad \forall \boldsymbol{v} \in V. \quad (3)$$

The state equation (3) is solved in the space $V = [H^1_{\circlearrowleft}(\Omega)]^2$ of the $H^1(\Omega)$-vector functions[1] satisfying periodic boundary conditions along the cell boundary, $\partial\Omega$, according to the asymptotic homogenization theory.

Inverse homogenization topology optimization TO searches the optimal distribution of a material inside a design domain, Ω, targeting prescribed objectives under a set of physical and design constraints. In such a context, it is customary to model the distribution of the material in Ω by means of a function, $\mathbf{1}_{\Omega^{mat}}$, which indicates the portions of the domain where the material is present or not, being

$$\mathbf{1}_{\Omega^{mat}}(\boldsymbol{x}) = \begin{cases} 1 & \text{for } \boldsymbol{x} = (x_1, x_2) \in \Omega^{mat} \\ 0 & \text{for } \boldsymbol{x} = (x_1, x_2) \in \Omega \backslash \Omega^{mat}, \end{cases} \quad (4)$$

with Ω^{mat} the subset of material points in Ω. The indicator function $\mathbf{1}_{\Omega^{mat}}$ allows to generalize the constant stiffness tensor in (1) to a quantity varying in Ω, so that E is replaced by

$$E_{\mathbf{1}}(\boldsymbol{x}) = \mathbf{1}_{\Omega^{mat}}(\boldsymbol{x}) E^0, \quad (5)$$

with $E^0 \in \mathbb{R}^{3\times 3}$ the stiffness tensor of the selected isotropic material. The indicator function assigns non-zero stiffness values only to the portion of the domain occupied by material, the full-material configuration in (1) being recovered for $\Omega^{mat} \equiv \Omega$.

From a computational viewpoint, function $\mathbf{1}_{\Omega^{mat}}(\boldsymbol{x})$ enables the solution of the problem of interest to the material domain Ω^{mat}, while setting the equations in the whole design domain Ω. In practice, the Boolean function $\mathbf{1}_{\Omega^{mat}}$ is regularized by introducing the continuous auxiliary function ρ, which models the density material distribution inside the design domain Ω

[1] Throughout the paper, we adopt standard notations for the function spaces following [38]

[23]. In particular, function ρ takes values in $[0,1]$, where $\rho(\boldsymbol{x}) = 1$ identifies solid material points, while $\rho(\boldsymbol{x}) = 0$ corresponds to void. Vice versa, intermediate density values ($0 < \rho(\boldsymbol{x}) < 1$) correspond to a non-physical material state. In order to limit the presence of such intermediate densities, we resort to the well-known Solid Isotropic Material with Penalization (SIMP) approach [23], which leads us to replace the stiffness tensor in (5) with

$$E_\rho(\boldsymbol{x}) = \rho^p(\boldsymbol{x}) E^0, \tag{6}$$

where $p > 0$ is a penalization exponent.
Thus, a generic SIMP-based TO approach can be stated as the following constrained minimization problem:

$$\min_\rho J(\boldsymbol{w}(\rho), \rho) \quad : \quad \begin{cases} a_\rho(\boldsymbol{w}(\rho), \boldsymbol{v}) = f_\rho(\boldsymbol{v}) \quad \forall \boldsymbol{v} \in \mathcal{V} \\ \underline{\boldsymbol{c}} \leq \boldsymbol{c}(\boldsymbol{w}(\rho), \rho) \leq \bar{\boldsymbol{c}} \\ \underline{\rho} \leq \rho \leq 1, \end{cases} \tag{7}$$

where $J(\cdot, \rho)$ is the objective functional; the first constraint models the physics underlying the minimization process, with $\boldsymbol{w}$ and $\boldsymbol{v}$ the trial and the test function in $\mathcal{V}$, respectively; the second constraint introduces a lower and an upper control ($\underline{\boldsymbol{c}}$ and $\bar{\boldsymbol{c}}$, respectively) onto the physical and/or design quantities collected in $\boldsymbol{c}(\cdot, \rho)$; the third inequality imposes an admissible range for ρ, the null value being replaced by $\underline{\rho} > 0$ to avoid numerical drawbacks.
In general, TO problem (7) is non-convex, and the uniqueness of the minimum can be ensured only by introducing a sufficient number of constraints.

As regards the TO problem applied to the design of stents, we particularize problem (7) as

$$\min_\rho J_S(\boldsymbol{u}^*(\rho), \rho) \quad : \quad \begin{cases} a_\rho^{ij}(\boldsymbol{u}^{*,ij}(\rho), \boldsymbol{v}) = f_\rho^{ij}(\boldsymbol{v}) \quad \forall \boldsymbol{v} \in \mathcal{V},\ ij \in \mathcal{I} \\ \underline{\boldsymbol{E}}_{\mathcal{C}} \leq \boldsymbol{E}^H_{\mathcal{C},\rho}(\boldsymbol{u}^*(\rho)) \leq \overline{\boldsymbol{E}}_{\mathcal{C}} \\ \underline{\rho} \leq \rho \leq 1, \end{cases} \tag{8}$$

where $\boldsymbol{u}^*(\rho)$ collects the fluctuation displacement components $\boldsymbol{u}^{*,ij}(\rho)$ in (3); $\boldsymbol{E}^H_{\mathcal{C},\rho}(\boldsymbol{u}^*(\rho))$ gathers the homogenized stiffness tensor components

$$E^H_{qrst,\rho}(\boldsymbol{u}^{*,qr}, \boldsymbol{u}^{*,st}) = \frac{1}{|\Omega|} \int_\Omega \rho^p [\boldsymbol{\sigma}(\boldsymbol{u}^{0,qr}) - \boldsymbol{\sigma}(\boldsymbol{u}^{*,qr})] : [\boldsymbol{\varepsilon}(\boldsymbol{u}^{0,st}) - \boldsymbol{\varepsilon}(\boldsymbol{u}^{*,st})] d\Omega,$$

constraining the design process, with $qrst \in \mathcal{I}^* \subseteq \{ijkl : ij, kl \in \mathcal{I}\}$, and where the dependence of $\boldsymbol{u}^{*,ij}(\rho)$ on ρ has been dropped to simplify the notation; vectors $\underline{\boldsymbol{E}}_{\mathcal{C}}$ and $\overline{\boldsymbol{E}}_{\mathcal{C}}$ provide the lower and upper bounds associated with the components $E^H_{qrst,\rho}$.
Since we are interested in controlling the contact area between the stent and the luminal surface of the vessel, we select the goal functional in (8) as the

quadratic deviation between a target volume fraction, V_f, and the actual volume of the structure, namely

$$J_S(\boldsymbol{u}^*, \rho) = J_S(\rho) = \left(\frac{1}{|\Omega|} \int_\Omega \rho d\Omega - V_f \right)^2. \tag{9}$$

In particular, minimizing the volume of the stent unit cell leads to choose $V_f = 0$ in (9) so that $J_S(\rho)$ simplifies to $|\Omega|^{-1} \int_\Omega \rho d\Omega$.
The physical model constraining the TO in (8) coincides with the SIMP variant of equation (3) for the displacement fluctuations in the unit cell, being

$$\begin{aligned} a_\rho^{ij}(\boldsymbol{u}^{*,ij}, \boldsymbol{v}) &= \int_\Omega \rho^p \boldsymbol{\sigma}(\boldsymbol{u}^{*,ij}) : \boldsymbol{\varepsilon}(\boldsymbol{v}) d\Omega, \\ f_\rho^{ij}(\boldsymbol{v}) &= \int_\Omega \rho^p \boldsymbol{\sigma}(\boldsymbol{u}^{0,ij}) : \boldsymbol{\varepsilon}(\boldsymbol{v}) d\Omega, \end{aligned} \tag{10}$$

with $\mathcal{V} = V = [H^1_{\circlearrowleft}(\Omega)]^2$.

With a view to the discretization of the optimization problem (8), we resort to a finite element approximation for the design variable ρ, the displacement trial and the test functions, $\boldsymbol{u}^{*,ij}$ and $\boldsymbol{v}$. We partition the stent unit cell design domain Ω with a family of conforming tessellations $\{\mathcal{T}_h\}_h$, consisting of triangular elements K with h the maximum of the diameters h_K. In particular, here the discrete space selected for ρ coincides with the set of the Ω-periodic piecewise affine polynomials, $R_h = \{r_h \in C^0(\overline{\Omega}) : r_h\big|_K \in \mathbb{P}_1(K)\} \cap H^1_{\circlearrowleft}(\Omega)$, while the components $\boldsymbol{u}^{*,ij}$ of $\boldsymbol{u}^*$ and $\boldsymbol{v}$ are chosen in $V_h = [R_h]^2$, so that the discrete counterpart of (8) can be expressed as

$$\min_{\rho_h} J_S(\rho_h) \quad : \quad \begin{cases} a^{ij}_{\rho_h}(\boldsymbol{u}_h^{*,ij}, \boldsymbol{v}_h) = f^{ij}_{\rho_h}(\boldsymbol{v}_h) \quad \forall \boldsymbol{v}_h \in V_h, \ ij \in \mathcal{I} \\ \underline{\boldsymbol{E}}_{\mathcal{C}} \leq \boldsymbol{E}^H_{\mathcal{C},\rho_h}(\boldsymbol{u}_h^*) \leq \overline{\boldsymbol{E}}_{\mathcal{C}} \\ \underline{\rho} \leq \rho_h \leq 1. \end{cases} \tag{11}$$

Anisotropic adaptive finite element discretization To manage the discrete constrained optimization problem in (11), we adopt the recently proposed microSIMPATY algorithm [30], which combines SIMP inverse homogenization with an anisotropic mesh adaptation strategy. This approach allows overcoming some of the limitations hampering the use of the discrete SIMP formulation, in particular the ones related to the adopted approximation, such as the greyscale effect, the generation of jagged boundaries as well as of complex structures which are far from being manufacturable [39, 23]. Moreover, the use of an adaptive mesh ensures to limit the employment of filtering techniques in the design and the post-processing of the optimized layout, thus yielding an automatic and cost-effective design tool.

Anisotropic adapted meshes are recognized as an ideal instrument to model problems characterized by strong gradients along certain directions.

This is the case of the design of structures where the material density exhibits a sharp gradient along the solid/void interface. The benefits led by the employment of a customized mesh within the TO process have been widely investigated for applications both at the macro- and at the micro-scale [40, 41, 42, 43, 44, 45, 46].

The key role played by the gradient of the density function in the topology optimization of structures suggested selecting $\nabla\rho$ as a driving quantity for the adaptation of the computational mesh. With this aim, we adopt the well-known a posteriori recovery-based error estimator proposed by O.C. Zienkiewicz and J.Z. Zhu in [47, 48] to control the $H^1(\Omega)$-seminorm of the discretization error. In the case of the optimization of structures, we apply such an estimator to the density function. This leads us to replace the seminorm

$$|e_h(\rho)|_{H^1(\Omega)} = \left[\int_\Omega \left|\nabla\rho - \nabla\rho_h\right|^2 d\Omega\right]^{1/2} = \left[\sum_{K\in\mathcal{T}_h}\int_K \left|\nabla\rho - \nabla\rho_h\right|^2 dK\right]^{1/2} \tag{12}$$

with the computable value

$$\xi = \left[\sum_{K\in\mathcal{T}_h} \xi_K^2\right]^{1/2} = \left[\sum_{K\in\mathcal{T}_h}\int_K \left|\boldsymbol{\Xi}_P(\rho_h)\right|^2 dK\right]^{1/2}, \tag{13}$$

$\boldsymbol{\Xi}_P(\rho_h) = \boldsymbol{P}(\rho_h) - \nabla\rho_h$ being the recovered error. Quantities ξ and ξ_K denote the global and local error estimator; $\boldsymbol{P}(\rho_h)$ represents the so-called recovered gradient which surrogates the exact (unknown) gradient $\nabla\rho$ in (12), by averaging and/or projecting the discrete gradient $\nabla\rho_h$. Several recipes are available in the literature to define $\boldsymbol{P}(\rho_h)$ [48, 49, 50, 51, 52, 53]. MicroSIMPATY employs the recovery formula

$$\boldsymbol{P}(\rho_h)(\boldsymbol{x}) = [P_1(\rho_h)(\boldsymbol{x}), P_2(\rho_h)(\boldsymbol{x})]^T = |\Delta_K|^{-1}\sum_{T\in\Delta_K} |T|\ \nabla\rho_h\big|_T(\boldsymbol{x}) \quad \boldsymbol{x}\in K, \tag{14}$$

with $\Delta_K = \{T\in\mathcal{T}_h : T\cap K\neq\emptyset\}$ the patch of elements associated with K, and $|\Delta_K|$ the patch area. Recipe (14), coinciding with an area-weighted average of the discrete gradient across the elements in Δ_K, is here selected since it is straightforward to be computed, cost-effective, and it turns out to be instrumental to an easy generalization of estimator (13) to an anisotropic setting. Indeed, following [54], we consider the anisotropic counterpart of estimator ξ, given by

$$\eta = \left[\sum_{K\in\mathcal{T}_h} \eta_K^2\right]^{1/2},$$

with

$$\eta_K^2 = \frac{1}{\lambda_{1,K}\lambda_{2,K}}\sum_{i=1}^{2}\lambda_{i,K}^2(\boldsymbol{r}_{i,K}^T G_{\Delta_K}(\boldsymbol{\Xi}_P(\rho_h))\boldsymbol{r}_{i,K}). \tag{15}$$

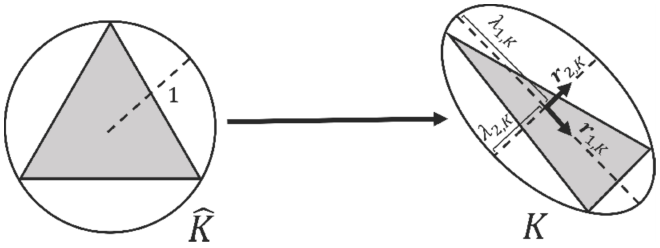

Figure 2: Sketch of the main quantities defining the anisotropy of element K.

In (15) the quantities $\lambda_{i,K}$ (with $\lambda_{1,K} \geq \lambda_{2,K} > 0$) and $\boldsymbol{r}_{i,K}$ fully characterize size, shape and orientation of the generic element K, providing the length and the direction of the semi-axes of the ellipse circumscribed to K (see Fig. 2). Furthermore, the symmetric positive semidefinite matrix G_{Δ_K}, with entries

$$\left[G_{\Delta_K}(\boldsymbol{\Xi}_P(\rho_h))\right]_{ij} = \sum_{T\in\Delta_K} \int_T \Xi_{P,i}(\rho_h)\ \Xi_{P,j}(\rho_h) dT \quad i,j = 1,2, \tag{16}$$

separates the components $\Xi_{P,k}(\rho_h) = P_k(\rho_h) - \partial_{x_k}\rho_h \in L^2(\Omega)$ $(k = 1, 2)$ of the recovered error, in order to be projected along the anisotropic directions. Finally, the scaling factor $(\lambda_{1,K}\lambda_{2,K})^{-1}$ guarantees the consistency of the anisotropic estimator η with the isotropic case in (13).

To exploit the estimator in (15) for the generatation of an anisotropic adapted mesh which captures the steep gradients characterizing ρ_h, we follow the metric-based approach in [55]. This technique allows us to predict the new local geometric features, $\mathcal{M}_K = \{\lambda^A_{i,K}, \boldsymbol{r}^A_{i,K}\}_{i=1,2}$ for each $K \in \mathcal{T}_h$, constituting the global metric $\mathcal{M} = \{\mathcal{M}_K\}_{K\in\mathcal{T}_h}$ associated with the new adapted mesh. To define $\mathcal{M}_K$, we employ an optimization procedure based on the following criteria:

(C1) setting of a user-defined accuracy, $\texttt{tol}_\eta$, onto the global estimator;

(C2) minimization of the mesh cardinality $\#\mathcal{T}_h$ (i.e., the number of the mesh elements);

(C3) equidistribution of the tolerance $\texttt{tol}_\eta$ throughout the mesh elements.

Criterion (C1) allows tuning the accuracy of the discrete solution according to the specific user's demands; the second rule implements a mesh cheapness requirement and is equivalent to maximize the area of each triangle; (C3) balances the estimator distribution across the new grid, imposing

$$\eta^2_K = \frac{\texttt{tol}^2_\eta}{\#\mathcal{T}_h}. \tag{17}$$

To guarantee the minimization of the mesh cardinality, we rescale the local estimator in (15) with respect to the area of the patch, so that

$$\eta_K^2 = C_K \lambda_{1,K} \lambda_{2,K} \left[s_K \left(\boldsymbol{r}_{1,K}^T G_{\Delta_K}^*(\boldsymbol{\Xi}_P) \boldsymbol{r}_{1,K} \right) + \frac{1}{s_K} \left(\boldsymbol{r}_{2,K}^T G_{\Delta_K}^*(\boldsymbol{\Xi}_P) \boldsymbol{r}_{2,K} \right) \right],$$

with C_K an explicitly computable constant, $s_K = \lambda_{1,K}/\lambda_{2,K} \geq 1$ the aspect ratio of the element K, measuring the deformation of the triangle (with $s_K = s_K^{\Delta} = 1$ corresponding to an equilateral triangle), $G_{\Delta_K}^*(\boldsymbol{\Xi}_P) = G_{\Delta_K}(\boldsymbol{\Xi}_P)/|\Delta_K|$ the scaled counterpart of the matrix in (16). We observe that the dependence of the recovered error on ρ_h has been dropped.
The equivalence between the mesh cardinality minimization and the element area maximization, combined with equality (17), leads us to solve the following constrained minimization problem on each element $K \in \mathcal{T}_h$:

$$\min_{s_K, \mathbf{r}_{i,K}} \mathcal{I}_K\big(s_K, \{\mathbf{r}_{i,K}\}_{i=1,2}\big) : \begin{cases} \boldsymbol{r}_{i,K} \cdot \boldsymbol{r}_{j,K} = \delta_{ij} \\ s_K \geq 1, \end{cases} \tag{18}$$

with

$$\mathcal{I}_K\big(s_K, \{\mathbf{r}_{i,K}\}_{i=1,2}\big) = s_K \left(\boldsymbol{r}_{1,K}^T G_{\Delta_K}^*(\boldsymbol{\Xi}_P) \boldsymbol{r}_{1,K} \right) + \frac{1}{s_K} \left(\boldsymbol{r}_{2,K}^T G_{\Delta_K}^*(\boldsymbol{\Xi}_P) \boldsymbol{r}_{2,K} \right),$$

and δ_{ij} the Kronecker symbol.
Problem (18) admits an explicit solution $\{s_K^A, \boldsymbol{r}_{i,K}^A\}_{i=1,2}$, given by

$$s_K^A = \sqrt{g_{1,K}/g_{2,K}}, \quad \boldsymbol{r}_{1,K}^A = \boldsymbol{g}_{2,K}, \quad \boldsymbol{r}_{2,K}^A = \boldsymbol{g}_{1,K}, \tag{19}$$

where $\{g_{i,K}, \boldsymbol{g}_{i,K}\}_{i=1,2}$ denote the eigenpairs associated with matrix $G_{\Delta_K}^*(\boldsymbol{\Xi}_P)$ [55]. Relation (17) is finally exploited to derive the two optimal anisotropic lengths $\lambda_{1,K}^A$ and $\lambda_{2,K}^A$ from the aspect ratio s_K^A in (19), thus obtaining

$$\lambda_{1,K}^A = g_{2,K}^{-1/2} \left(\frac{\texttt{tol}_\eta^2}{2\,\#\mathcal{T}_h\, C_K} \right)^{1/2}, \quad \lambda_{2,K}^A = g_{1,K}^{-1/2} \left(\frac{\texttt{tol}_\eta^2}{2\,\#\mathcal{T}_h\, C_K} \right)^{1/2}. \tag{20}$$

The optimal lengths $\lambda_{i,K}^A$ in (20) and directions $\boldsymbol{r}_{i,K}^A$ in (19) constitute the optimal metric $\mathcal{M}_K$ associated with triangle K. These local metrics define the global metric $\mathcal{M}$ to be passed as an input to a metric-based mesh generator, as detailed in the next section.
The interested reader can find more insights about the whole adaptive process in [55].

2.1.2 MicroSIMPATY algorithm for the design of engineered stent unit cells

In this section, we focus on the main software tools used to implement microSIMPATY algorithm. Concerning the solution to problem (11), we resort

to: FreeFEM [56] as a finite element solver to approximate the state equations constraining the optimization process; the large-scale nonlinear Interior Point OPTimizer (IPOPT) [57] to carry out the constrained minimization; the mesh generator BAMG (Bidimensional Anisotropic Mesh Generator) integrated in FreeFEM to build the adapted mesh [58]. In particular, BAMG requires the metric $\mathcal{M}$ at the vertices, $\boldsymbol{z}$, of the mesh $\mathcal{T}_h$. For this reason, we convert the piecewise constant metric, $\mathcal{M} = \{\mathcal{M}_K\}$, defined by (19) - (20) into a piecewise linear field, $\widetilde{\mathcal{M}} = \{\widetilde{\mathcal{M}}_{\boldsymbol{z}}\}$, by using the average

$$\widetilde{\mathcal{M}}_{\boldsymbol{z}} = \frac{1}{|\Delta_{\boldsymbol{z}}|} \sum_{K \in \Delta_{\boldsymbol{z}}} |K| \, \mathcal{M}_K, \tag{21}$$

with $\Delta_{\boldsymbol{z}}$ the patch of elements associated with vertex $\boldsymbol{z}$.
As a last step, we further improve metric $\widetilde{\mathcal{M}}$ in order to avoid any numerical bias in the structural mechanical analysis [59]. Indeed, it is known that elongated elements may influence the reliability of such an analysis, leading to an under-/over-estimation of the quantities involved in the design process. To overcome this issue, we adopt the strategy proposed in [60] where highly stretched triangles are alternated to isotropic elements. The idea is to exploit the capability of an anisotropic mesh of sharply tracking the layout boundaries, while preserving shape-regular triangles in the internal part of the structure to keep the computed mechanical quantities unbiased. We refer to such hybrid computational tessellation as to a graded mesh.

The overall design procedure supported by microSIMPATY is listed in the following algorithm.

Algorithm 1 microSIMPATY for engineered stent unit cells design

Input: $\mathtt{tol}_J$, $\mathtt{tol}_\eta$, $\mathtt{tol}_M$, $\mathtt{k}_{\max}$, $\underline{\rho}$, $\underline{\boldsymbol{E}}_{\mathcal{C}}$, $\overline{\boldsymbol{E}}_{\mathcal{C}}$, $\mathcal{I}^*$, V_f, $\rho_h^{(0)}$, $\mathcal{T}_h^{(0)}$
Set $\mathtt{k} = 0$, $\mathtt{err}_M = 1 + \mathtt{tol}_M$;
while $\mathtt{err}_M > \mathtt{tol}_M$ and $\mathtt{k} < \mathtt{k}_{\max}$ **do**
  $\tilde{\rho}_h^{(\mathtt{k}+1)} = \mathtt{IPOPT}(\rho_h^{(\mathtt{k})}, \mathcal{T}_h^{(\mathtt{k})}, V_f, \underline{\rho}, \underline{\boldsymbol{E}}_{\mathcal{C}}, \overline{\boldsymbol{E}}_{\mathcal{C}}, \mathcal{I}^*, \mathcal{G}, \nabla_\rho \mathcal{G}, \mathtt{tol}_J)$;
  $\rho_h^{(\mathtt{k}+1)} = \mathtt{filtering}(\tilde{\rho}_h^{(\mathtt{k}+1)}, \beta, r_f)$;
  $\mathcal{T}_h^{(\mathtt{k}+1)} = \mathtt{adaptation}(\mathcal{T}_h^{(\mathtt{k})}, \rho_h^{(\mathtt{k}+1)}, \mathtt{tol}_\eta)$;
  $\mathtt{err}_M = |\#\mathcal{T}_h^{(\mathtt{k}+1)} - \#\mathcal{T}_h^{(\mathtt{k})}| / \#\mathcal{T}_h^{(\mathtt{k})}$;
  $\mathtt{k} = \mathtt{k} + 1$
end while
$\tau = \rho_h^{(\mathtt{k})}$;
$E_\tau^H = \mathtt{homogenize}(\tau)$;
Output: τ, E_τ^H

The input parameters of Algorithm 1 are: three tolerance values and a maximum number of iterations, constraining the design process; the bounds characterizing the box inequalities in (11) together with the set of indices

$\mathcal{I}^*$ identifying the homogenized stiffness tensor components for the design process; the goal volume fraction involved in the definition of functional J_S in (9); the initial material density and mesh.
MicroSIMPATY alternates an optimization step (line 4), a filtering phase (line 5) and the anisotropic mesh adaptation procedure (line 6), within a **while** loop, controlled in terms of the stagnation of the relative mesh cardinality and of the maximum number, $\mathtt{k}_{\max}$, of allowed iterations.
Function `IPOPT` returns the new density distribution $\tilde{\rho}_h^{(\mathtt{k}+1)}$ obtained starting from the current design variable $\rho_h^{(\mathtt{k})}$ associated with mesh $\mathcal{T}_h^{(\mathtt{k})}$, in order to match tolerance $\mathtt{tol}_J$. In particular, vector $\mathcal{G}$ gathers the goal functional and the constrained quantities, namely,

$$\mathcal{G} = [J_S(\rho), \boldsymbol{E}^H_{\mathcal{C},\rho}]^T, \tag{22}$$

while $\nabla_\rho \mathcal{G}$ collects the associated sensitivities (see [44] for more details, where a Lagrangian approach is adopted to compute the derivative of the components of $\mathcal{G}$ with respect to ρ).
Concerning the filtering phase, we employ a differentiable variant of the Heaviside function, characterized by parameter β, and a Helmholtz-like filter with a radius equal to r_f [61, 62]. The action of the Heaviside function is to sharpen the layout boundary by removing the intermediate material densities (the larger β, the more clear-cut the boundary design). The Helmholtz-like filter smooths the irregularities and erases the thin features possibly arising along the structure boundary (the larger r_f, the more effective the smoothing action).
Successively, the filtered density $\rho_h^{(\mathtt{k}+1)}$ is used by function `adaptation` to compute the nodewise metric in (21) and to generate the new anisotropic adapted mesh.

MicroSIMPATY algorithm returns the optimized layout τ together with the associated homogenized stiffness tensor E^H_τ of components

$$E^H_{ijkl,\tau}(\boldsymbol{u}^{*,ij}, \boldsymbol{u}^{*,kl}) = \frac{1}{|\Omega|}\int_\Omega \tau^p[\boldsymbol{\sigma}(\boldsymbol{u}^{0,ij}) - \boldsymbol{\sigma}(\boldsymbol{u}^{*,ij})] : [\boldsymbol{\varepsilon}(\boldsymbol{u}^{0,kl}) - \boldsymbol{\varepsilon}(\boldsymbol{u}^{*,kl})]d\Omega,$$

for ij, $kl \in \mathcal{I}$.

2.1.3 Designing innovative stent base cells with microSIMPATY: an example

In this section, we investigate the performance of Algorithm 1 on a first case study, while referring to Sect. 3.1 for different optimization scenarios. We carried out the design phase in a non-dimensional setting, while we introduce dimensional units for the verification phases addressed in Sections 3.2 and 3.3.

Concerning the physical background, we identify the design domain Ω with the square $(0, 10)^2$. We consider an isotropic reference material with

constitutive law $\sigma(\boldsymbol{u}) = 2\mu\,\varepsilon(\boldsymbol{u}) + \lambda\,\mathrm{tr}(\varepsilon(\boldsymbol{u}))\mathrm{I}$, being $\lambda = E_Y\nu/[(1+\nu)(1-2\nu)]$ and $\mu = E_Y/[2(1+\nu)]$ the Lamé coefficients, $E_Y = 60$ and $\nu = 0.33$ the Young modulus and the Poisson ratio, $\mathrm{tr}(\cdot)$ the trace operator, and I the identity tensor. Finally, the SIMP penalization exponent p in (10) is set to 4.

The optimization in line 4 of Algorithm 1 is performed by setting $\rho_h^{(0)} = |\sin(2\pi x/8)\sin(2\pi y/8)|$ on an initial structured grid, $\mathcal{T}_h^{(0)}$, with 5000 elements, $V_f = 0$, $\underline{\rho} = 10^{-4}$, $\mathcal{I}^* = \{1111, 1122\}$, $\underline{\boldsymbol{E}}_{\mathcal{C}} = [\underline{E}_{1111}, \underline{E}_{1122}]^T = [0.25, 0.50]^T$, $\overline{\boldsymbol{E}}_{\mathcal{C}} = [\overline{E}_{1111}, \overline{E}_{1122}]^T = [1.0, 1.0]^T$, $\mathcal{G}$ as in (22) with $\boldsymbol{E}^H_{\mathcal{C},\rho} = [E^H_{1111,\rho}, E^H_{1122,\rho}]^T$, and $\mathtt{tol}_J = 10^{-6}$. Function $\rho_h^{(0)}$, characterized by uniformly distributed circular holes, is expected to promote free-form features in the final optimized structure. Components $E^H_{1111,\rho}$ and $E^H_{1122,\rho}$ are considered to generate the proof-of-concept design, although any other component of the homogenized stiffness tensor could be included in $\boldsymbol{E}^H_{\mathcal{C},\rho}$, according to the specific design requirement.

The filtering consists of a sharpening of the material/void interface, followed by a smoothing of the possible irregularities along such a boundary at each iteration. With this aim, the parameter for the Heaviside function is chosen as $\beta = 2$, while the filtering radius r_f for the Helmholtz filter is set to 0.06 and reduced by a factor of 1.5 for each $\mathtt{k}$.

The anisotropic mesh adaptation is tuned by the tolerance $\mathtt{tol}_\eta = 10^{-3}$. Finally, the design iterations are controlled by parameters $\mathtt{tol}_M$ and $\mathtt{k}_{\max}$ selected equal to 10^{-5} and 5, respectively.

MicroSIMPATY algorithm delivers the stent unit cell of Fig. 3, panel (A) (referred to as Design 1 in the sequel) after 5 iterations, completed in 395 seconds[2]. The output volume fraction is 6.11% of the initial design domain volume. This justifies the very thin struts and the consequent low contact area in the final cell layout. The mesh adaptation procedure yields a final grid consisting of 3106 elements, whose maximum deformation is confined along the cell boundary and corresponds to $s_K^{\max} = 78.22 \gg s_K^{\Delta}$.
The homogenized stiffness tensor associated with Design 1 is

$$E^H_\tau = \begin{pmatrix} 0.497 & 0.507 & 0.010 \\ 0.507 & 0.545 & 0.013 \\ 0.010 & 0.013 & 0.046 \end{pmatrix}, \tag{23}$$

which corroborates that the two box constraints in (11) are matched, approaching the lower bound in both cases.
Finally, we observe that the converge history of the objective functional, of the box constraints, and of the mesh cardinality are very similar to the ones in [63, Fig. 3].

[2]The computations have been run on a MacBook Pro laptop (2022), equipped with Apple M1-Pro CPU (2.064 – 3.228 GHz) and 32 GBs of RAM.

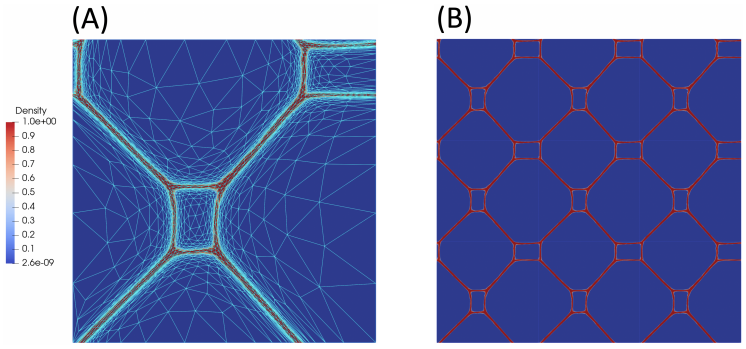

Figure 3: Design 1. Optimized unit cell τ and associated graded mesh (A); 3×3 periodic lattice (B).

2.2 3D stent geometry reconstruction

This section focuses on the second block of the workflow of Fig. 1 by describing how to obtain the 3D stent geometry from the 2D unit cell topologically optimized by microSIMPATY algorithm. In practice, we resort to a 4-step procedure implemented with Hypermesh software (Altair Engineering, Troy, MI, USA), which receives as input the `.stl` file of the optimized layout τ. The process is sketched in Fig. 4 and consists in:

- the repositioning and the uniform scaling of the 2D unit cell by a factor equal to $s = \pi D/n$, with D the diameter of the selected cylindrical surface and n the number of cell repetitions along the device circumference (panel (A)). This procedure is employed to avoid convergence issues of the nonlinear structural mechanics simulations of stent crimping;
- the projection of the 2D cell onto a cylindrical surface with diameter D = 7 mm (panel (B));
- the repetition of the projected cell $n = 10$ times along the circumferential (θ) and 5 times along the axial (z) direction, respectively (panel (C));
- the extrusion of the surface lattice along the negative radial direction (r) to assign a constant strut thickness equal to 0.2 mm (panel (D)), which is a typical value for commercially available femoral stents [64].

2.3 Structural response of the stent

The 2D unit cells yielded by microSIMPATY are generated under a linear elastic regime, without accounting for nonlinearites involving large deformations, structural instability, super-elastic Nickel-Titanium (NiTi) material

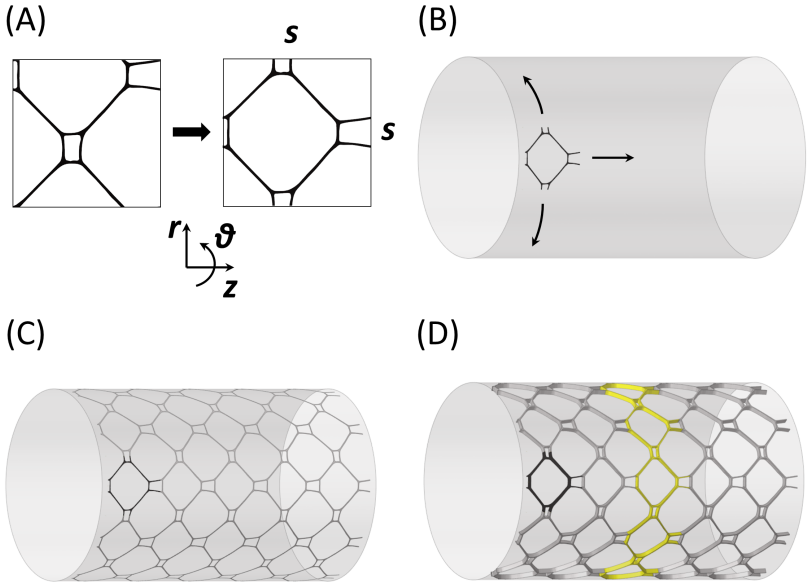

Figure 4: 3D stent geometry reconstruction procedure: repositioning and scaling (A), projection (B), repetition (C), and extrusion (D). The adopted reference cylindrical coordinate system is highlighted in panel (A). Only half stent is represented in panels (C) and (D).

behavior and contact conditions. However, in the third block of the workflow of Fig. 1, we carry out a nonlinear FE analysis of a complete crimping cycle, in order to accurately characterize the structural performance of the new stent designs.

Hypermesh in conjunction with Abaqus/Standard (Dassault Systèmes Simulia Corp., Johnston, RI, USA) is used to implement the FE models. The structural FE simulations involve two components, namely the self-expandable NiTi stent and the crimping cylinder. The 3D stent geometry is discretized in Abaqus with C3D8R hexahedral elements with reduced integration, considering 4 and 10 elements across the strut width and thickness, respectively, in accordance to previous computational studies [65, 66]. The mechanical behavior of NiTi material is described by a super-elastic constitutive model [67], retrieving the material parameters from [68]. The crimping cylinder is modeled as a rigid cylindrical surface, with a diameter of 7.5 mm, and is discretized by using rigid surface elements SFM3D4R [69].

The structural FE analysis is carried out by using an implicit solver to deal with the nonlinear equations of static equilibrium, running on 6 computing cores of a workstation equipped with Intel® Core™ i7-8700 and 32 GB RAM. The analysis involves the crimping and the expansion steps. In the crimping step (Fig. 5, panel (A)), negative radial displacements are assigned to the nodes of the crimping cylinder, thus reducing the diameter

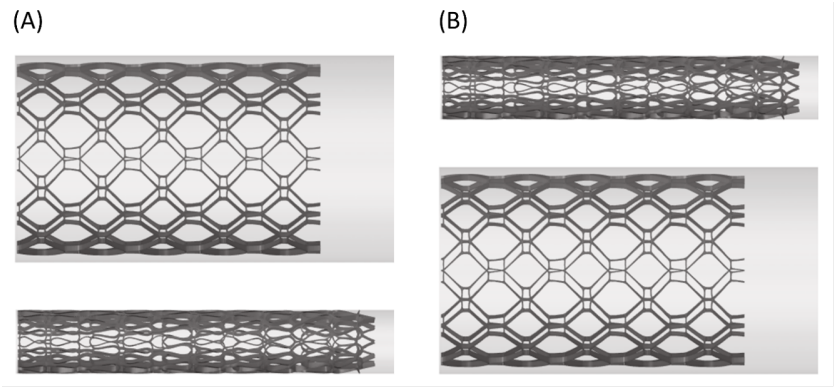

Figure 5: FE structural analysis of a complete crimping step. (A) Crimping step. (B) Expansion step.

from 7.5 mm to 2.3 mm (corresponding to a catheter of 7 Fr), whereas in the expansion step (Fig. 5, panel (B)) the crimping cylinder is released to the initial diameter. The nodes on one boundary section of the stent (i.e., the left boundary section in Fig. 5) are constrained along the axial direction z. Contact between the stent and the crimping cylinder, and self-contacts between the stent struts are modeled with a pure master-slave contact algorithm, by assuming a friction coefficient of 0.1 and a hard-contact pressure-overclosure relationship [70]. Finally, artificial damping is added to stabilize the nonlinear simulations, in order to control that the ratio between the related dissipation energy and the total internal energy is less than 5%.

To evaluate the structural performance of the new stent designs, we refer to the design requirements listed in the introduction of Section 2, by considering the following FE outputs:

- the peak maximum principal strain of the stent. With reference to the limit value, the material elongation at break is set to 18%, in accordance to previously conducted tensile tests on NiTi specimens [71];
- the radial force (per unit length), which is computed as the sum of the generated contact normal forces along the radial direction divided by the initial stent length;
- the stent foreshortening, which is computed as $(l - l_0)/l_0$, where l_0 and l are respectively the initial stent length and the stent length in correspondence with the variable crimping diameter;

In order to avoid undesirable boundary effects, the FE outputs are computed considering only the central stent cells as highlighted in Fig. 4, panel (D).

2.4 Hemodynamic features of the stent

As a last step in the workflow in Fig. 1, we investigate the impact of the new stents on the arterial hemodynamics, by performing transient, laminar CFD simulations on the stent designs successfully tested by the FE structural analysis in the previous section. In detail, we place the new devices in an idealized (cylindrical) geometry, modeling the superficial femoral artery with a diameter of 6 mm. To avoid boundary effects, a stent portion approximately 13 mm long, located at 2 and 5 diameters from the model inlet and outlet section, respectively, is here considered.

The stented arterial geometry is discretized using Fluent Meshing (Ansys Inc., Canonsburg, PA, USA). According to [72, 64], the fluid domain is discretized with tetrahedral elements in the bulk flow and with five layers of high-quality prismatic cells near the luminal surface. The computational mesh is refined close to the stent struts to sharply detect the small-scale flow features between struts regions (we refer to [64] for a sensitivity analysis of the mesh with respect to the element size).

The finite volume-based commercial code Fluent (Ansys Inc., Canonsburg, PA, USA) is adopted to numerically solve the discretized unsteady Navier-Stokes equations, by assuming the blood as an incompressible, homogeneous fluid, with constant density equal to 1060 kg m^{-3}. The shear-thinning blood behaviour is modelled using the non-Newtonian Carreau model, describing the relationship between viscosity and shear rate $\dot{\gamma}$ as follows:

$$\mu(\dot{\gamma}) = \mu_\infty + (\mu_0 - \mu_\infty)[1 + (\Upsilon\dot{\gamma})^2]^{\frac{m-1}{2}} \tag{24}$$

where μ_∞= 0.0035 Pa s and μ_0 = 0.25 Pa s are the infinite and zero shear rate limit viscosities, respectively, Υ = 25 s is the relaxation time constant, and m = 0.25 is the power law index [73]. Concerning the boundary conditions, at the inlet section we prescribe a patient-specific velocity waveform, derived from Doppler ultrasound images, in terms of a parabolic profile [64]. In detail, the pulsatile inflow waveform amplitude is scaled with respect to the inlet diameter to ensure a physiological mean flow rate value. A reference pressure is imposed at the outflow section. The no-slip condition is applied to the vessel and stent walls, assumed as rigid in the context of CFD simulations. Further details on the numerical setting are exhaustively provided in [64].

The hemodynamic characteristics of the stent design are evaluated according to the fourth design requirement listed in the introduction of Section 2. In detail, the local hemodynamics along the stented region is analyzed in terms of the canonical quantity TAWSS (Time-Averaged Wall Shear Stress), namely the average WSS magnitude value along the cardiac cycle. In addition, we investigate the WSS topological skeleton features at the stented region, due to the recently emerged link to atherogenesis [74]. Following a recently proposed Eulerian-based approach [75], the divergence of the nor-

Table 1: Designs 1 – 5. MicroSIMPATY parameters distinguishing the optimized unit cells.

	$\underline{E}_{1111}$	$\bar{E}_{1111}$	$\underline{E}_{1122}$	$\bar{E}_{1122}$	r_f
Design 1	0.25	1.00	0.50	1.00	0.060
Design 2	0.60	0.75	0.15	0.25	0.025
Design 3	0.25	1.00	-0.40	-0.20	0.050
Design 4	0.50	1.00	0.75	1.25	0.075
Design 5	0.25	0.80	0.50	0.90	0.060

malized WSS vector field, σ_{WSS}, is used to identify the WSS contraction and expansion areas at the stented vessel surface. Then, the amount of variation in WSS contraction/expansion action along the cardiac cycle $[0, T]$ is quantified by the Topological Shear Variation Index (TSVI), with

$$\text{TSVI} = \Big[\frac{1}{T} \int_0^T \big[\nabla \cdot \sigma_{\text{WSS}} - \overline{\nabla \cdot \sigma_{\text{WSS}}}\big]^2 dt \Big]^{1/2}, \tag{25}$$

namely the root-mean-square deviation of the divergence of σ_{WSS} with respect to the associated spatial average [76, 74, 77].

3 Results

In this section, we consider five proof-of-concept stent designs and analyze the associated structural and fluid dynamics performance.

3.1 TO-based stent unit cell designs

We employ Algorithm 1 for the design of four new stent unit cells, in addition to Design in Section 2.1. The optimization phase essentially preserves the selected functional, the material properties, and the input parameters to microSIMPATY as for Design 1, except for the lower and upper bounds of the components of the stiffness tensor ($\underline{\boldsymbol{E}}_{\mathcal{C}}$, $\overline{\boldsymbol{E}}_{\mathcal{C}}$) in (11), and for the starting radius r_f of the Helmholtz filter, differently set for each design as summarized in Table 1. In detail, Design 2 is the output of the optimization when microSIMPATY is applied to narrow intervals for E^H_{1111,ρ_h} and E^H_{1122,ρ_h}; Design 3 is the output when imposing negative values of E^H_{1122,ρ_h} in the optimization strategy, with a view to an auxetic stent design; Designs 4 and 5 are considered to investigate the sensitivity of the final layout with respect to the range for E^H_{1111,ρ_h} and E^H_{1122,ρ_h}.

The optimized densities τ delivered by microSIMPATY for the five parameter settings are shown in Fig. 6, together with the associated geometries (where the clear-cut designs τ are repositioned and converted into the `.stl`

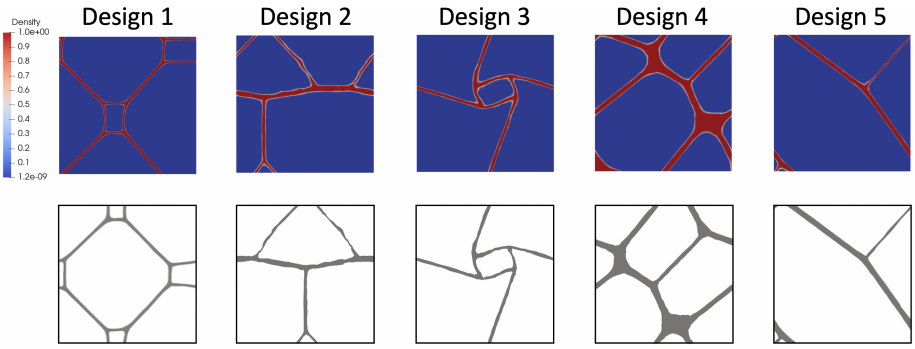

Figure 6: Optimized unit cells τ (top) and associated `.stl` geometries (bottom) for Designs 1 – 5 (left-right).

Table 2: Designs 1–5. Volume fraction characterizing the final microSIMPATY layout.

	Volume fraction (%)
Design 1	6.11
Design 2	7.52
Design 3	6.55
Design 4	16.55
Design 5	5.56

format). From Fig. 6, the heterogeneity of the stent cells is evident. Furthermore, the originality of the optimized layouts stands out when compared with common designs currently employed in the production of commercial stents [3]. By visual inspection, it turns out that: Designs 2 and 3 exhibit thinner connection struts, essentially aligned with the horizontal and vertical directions; Designs 4 and 5 generate more closely connected structures and are more similar to Design 1, by offering a diagonal rotation and stretching of the cell unit of the latter.

Some quantitative comments on the output of microSIMPATY are in order. We first consider the converged objective functional, namely the minimization of the contact area between the stent and the arterial walls, expressed in terms of material volume fraction (see Table 2). The final layouts feature a 5.6 - 7.5 % volume fraction of the initial design domain, consistently with the very thin struts characterizing the designs in Fig. 6. In these cases, the significant minimization of J_S can be ascribed to the wide ranges selected for the constraints. Conversely, Design 4 represents an exception, with a final 16.55 % volume fraction, which is promoted by the larger values enforced for E^H_{1122,ρ_h} (see Table 1).

As a last check, we provide the explicit expression for the homogenized

stiffness tensor for the cells, given by (23) and

$$\text{Design 2} \qquad E_\tau^H = \begin{pmatrix} 0.600 & 0.151 & -0.002 \\ 0.151 & 0.099 & 0.0003 \\ -0.002 & 0.0003 & 0.009 \end{pmatrix},$$

$$\text{Design 3} \qquad E_\tau^H = \begin{pmatrix} 0.289 & -0.200 & -0.077 \\ -0.200 & 0.196 & 0.066 \\ -0.077 & 0.066 & 0.025 \end{pmatrix},$$

$$\text{Design 4} \qquad E_\tau^H = \begin{pmatrix} 0.824 & 0.772 & 0.066 \\ 0.772 & 0.848 & 0.057 \\ 0.066 & 0.057 & 0.368 \end{pmatrix},$$

$$\text{Design 5} \qquad E_\tau^H = \begin{pmatrix} 0.510 & 0.519 & -0.376 \\ 0.519 & 0.539 & -0.384 \\ -0.376 & -0.384 & 0.298 \end{pmatrix}.$$

The optimized values $E^H_{1111,\tau}$ and $E^H_{1122,\tau}$ are compliant with the lower and upper bounds summarized in Table 1 for all the design cases. It is worth noticing that $E^H_{1122,\tau}$ is just above the lower bound (and just below the upper bound in the case of Design 3) since the optimization process reduces the volume fraction at the expense of stiffness, within the allowed ranges for the constrained components. This trend is less evident for $E^H_{1111,\tau}$ due to the wider range of admissible values.

3.2 Structural mechanics simulations

In this section, we carry out the FE structural analysis set in Section 2.3 on the 3D stent models associated with the 2D unit cells in Fig. 6. Virtual crimping is adopted to discriminate among the five stent layouts. For each stent model, the distributions of the maximum principal strain at the initial and at the minimum crimping diameter are presented in Fig. 7 (we refer also to Table 3 for corresponding quantitative data).

From virtual crimping, we observe that: Design 2 is subject to severe structural instability issues which do not allow for complete stent crimping (Fig. 7, panel (B)); Design 3 exhibits several auto-contacts between the stent struts at the beginning of the crimping, that prevent a further reduction of the catheter diameter and ultimately impede the finalization of the crimping procedure (Fig. 7, panel (C)); Design 4 reports structural integrity issues, with a peak of maximum principal strain larger than the value of elongation at break. On the contrary, it turns out that Designs 1 and 5 can be adequately crimped. In particular, with reference to Table 3, Designs 1 and 5 allow reaching the target minimum catheter diameter, 2.3 mm, whereas the other three devices fail. Moreover, Design 1 is characterized by the lowest

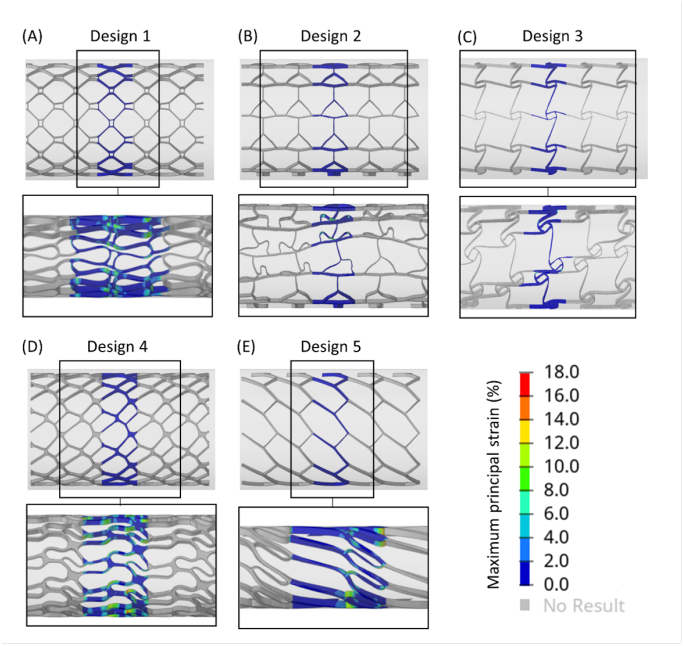

Figure 7: Designs 1–5. Maximum principal strain at the initial (top) and at minimum (bottom) crimping diameter. Half stent of each design is represented in section.

overall value of the peak maximum principal strain and, consequently, it has the lowest risk for structural failure throughout the device deployment procedure [18].

As a second level of investigation, radial force and foreshortening as a function of the crimping diameter are analyzed (see Fig. 8). A nonlinear trend shows up, to be ascribed to the combined effect of the material superelasticity and structural instabilities. Moreover, Designs 1 and 5, namely the only stents that completed the crimping step, exhibit a hysteresis cycle as it typically occurs in self-expandable NiTi devices. By analyzing Fig. 8 (panel (A)), we remark that Designs 4 and 5 attain the highest and the lowest values of the radial force at the beginning of the crimping step, respectively.

Table 3: Designs 1–5. Minimum crimping diameter and corresponding peak value of the maximum principal strain.

	Min crimping diameter (mm)	Peak max principal strain (%)
Design 1	2.3	10.0
Design 2	5.4	12.7
Design 3	5.3	11.1
Design 4	4.0	18.0
Design 5	2.3	15.0

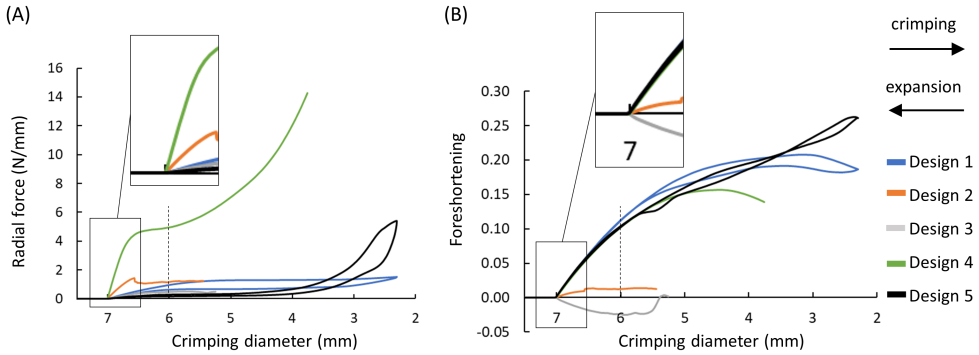

Figure 8: Designs 1–5. Radial force (per unit length) (A) and foreshortening (B) as a function of the crimping diameter. Details are shown for the initial part of the curves. The dotted line marks the intersection between the stent and a vessel with a constant diameter of 6 mm, throughout the expansion step.

Table 4: Designs 1 and 5. Radial force (per unit length) and foreshortening values at the crimping diameter of 6 mm in the expansion step.

	Radial force (N/mm)	Foreshortening
Design 1	0.65	0.112
Design 5	0.17	0.105

Interestingly, Design 1 and 5 show near constant values of the radial force for the range of crimping diameters equal to [5.5 mm, 2.3 mm] and [6 mm, 4 mm], respectively. In panel (B), we can appreciate that Designs 1, 4 and 5 exhibit near equal foreshortening values at the beginning of the crimping step, whereas Design 2 presents much lower values. Design 3 takes negative values with an inversion of the trend at the beginning of the crimping step, behaving as an auxetic structure.

Finally, the radial force and the foreshortening values at the diameter of 6 mm during virtual stent expansion are presented in Table 4, only for Designs 1 and 5 since they complete the entire crimping cycle. Markedly different radial force characterize the two designs.

3.3 CFD simulations

Based on the results of the structural analysis, Designs 1 and 5 emerge as potential candidates for innovative stent design. For this reason, CFD simulations for the evaluation of the hemodynamic performance of the stent models are confined to the devices built on Designs 1 and 5 only. The hemodynamic performance is evaluated in terms of the WSS-based quantities introduced in Section 2.4, namely TAWSS and TSVI, whose luminal distributions are mapped over the stented region in Fig. 9. The two designs

exhibit similar TAWSS distributions (Fig. 9, top, panels (A) and (B)), with low values located around the stent struts, and high values located in regions between the struts (i.e., in the stent unit cell central area). Moreover, both stent models present the highest TAWSS in the proximal segment, where an open cell configuration characterizes the stents ring. As for the TSVI luminal distribution, high variations in the WSS contraction/expansion action along the cardiac cycle are mainly located proximal and distal to the stent struts, according to previous observations in commercially available stents (Fig. 9, bottom, panels (A) and (B)) [72]. In both stent models, the highest TSVI values (> 5000 m^{-1}) are located at the stent peaks and valleys, and at the links between the stent rings. Conversely, lower TSVI values characterize the central region of stent unit cells. Overall, a co-localization between low TAWSS and high TSVI values in the proximity of the stent struts is observable in both stent models.

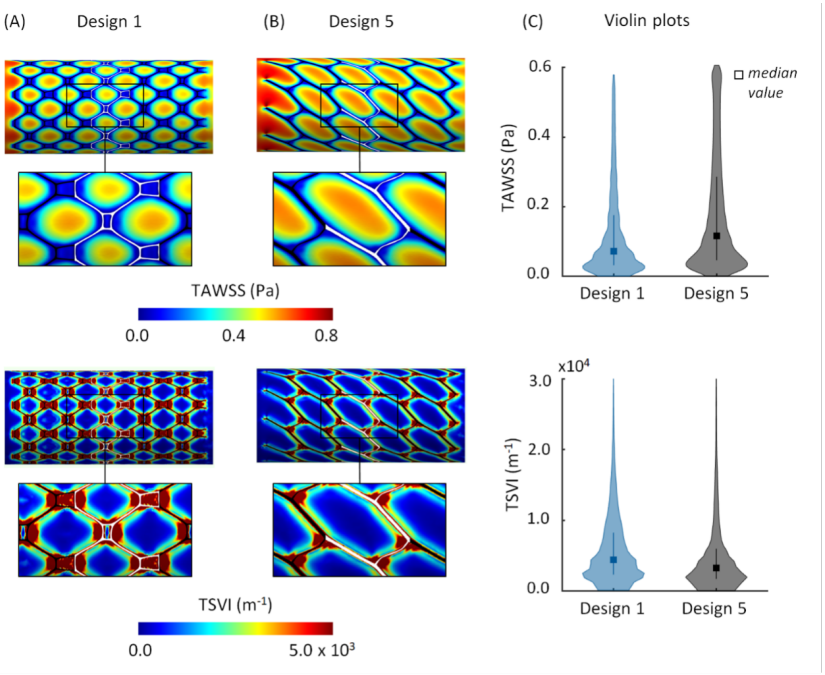

Figure 9: Color maps of TAWSS (top) and TSVI (bottom) along the luminal surface of stented region of Design 1 (A) and Design 5 (B). Violin plots (C) of TAWSS (top) and TSVI (bottom) for a single stent ring (white-highlighted in (A) and (B)).

Despite the observed similarities in TAWSS and TSVI luminal distributions, the extension of the luminal surface regions exposed to low TAWSS and high TSVI values is larger in the stent model based on Design 1. This is confirmed by the quantitative analysis of the distributions of TAWSS and TSVI on the luminal surface region around a single stent ring (see violin

plots in Fig. 9, panel (C)). In particular, the stent ring associated with Design 1 presents lower TAWSS and higher TSVI median values as compared to the model corresponding to Design 5 (0.07 [0.03 – 0.17] Pa versus 0.12 [0.05 – 0.29] Pa, and 4408 [2359 – 8237] m^{-1} versus 3290 [1750 – 5987] m^{-1} , respectively).

4 Discussion

In the following, we critically examine the results of the proposed TO-based strategy for peripheral stents design, with a view to a possible practical employment and to a future enhancement of the workflow.

4.1 Innovation onto the state of the art

The inverse homogenization TO-based computational framework in Section 2.1 offers a disruptive workflow. In the first step of the process, microSIMPATY algorithm is employed to systematically yield unconventional unit cells, instrumental to the design of new self-expandable femoral stents (second step). Compared with the contributions in the literature [24, 25] where TO drives the proposal of new stent designs, the approach here introduced resorts to inverse homogenization to efficiently deal with the interplay between the unit cell prototyping and the properties of the whole device. In addition, the process turns out to be general, going beyond the design of auxetic stents as addressed in [26, 27]. A further innovative feature characterizing the new pipeline is represented by the employment of computational meshes highly customized to the TO process. This peculiarity makes the whole design process time- and cost-effective, and promotes completely original layouts.

In the two last steps of the workflow, a verification is accomplished to determine the biomechanical performance guaranteed by the new stent designs, focusing on the actual geometric, structural and hemodynamic properties. In particular, the new workflow also takes into account the minimum requirement for usability, by simulating the device crimping up to the catheter diameter.

4.2 New stent designs: the topology optimization process

The considerable versatility of the new design process is confirmed by the high heterogeneity exhibited by the proof-of-concept layouts in Section 3.1, both in terms of topology and mechanical/hemodynamic performance (see Sections 3.2 and 3.3). This variety of solutions is unlocked by the different choices for the objective functional and for the constraints of the optimization problem (11), as well as by the numerical parameters involved in Algorithm 1 (see, e.g., [63, 43]). In this context, a key role is played by the

selected ranges for the homogenized stiffness tensor components, promoting the proposal of original unit cells when compared with the designs commonly employed in the stent production. From a mathematical viewpoint, the heterogeneity of the topologically optimized layout can be ascribed to the non-convexity of problem (11), namely to the existence of several local minima [23]. Moreover, the adoption of an anisotropic mesh adaptation in the design process leads to fully sustainable computations. For instance, the prototyping of a new stent unit cell requires, on average, 15 minutes on a standard laptop.

In more detail, the analysis carried out in Section 3.1 highlights that large values for the homogenized stiffness tensor components promote high volume fractions (i.e., a high contact area), while wide ranges for the constraints lead to a relevant reduction of the volume fraction (i.e., a low contact area). The obtained volume fractions are in the range $5 - 7\%$ (except for Design 4 with 16.55%), which are smaller with respect to those of some commercially available femoral stents, such as the EverFlex stent (EV3, Medtronic, Dublin, Ireland), characterized by a volume fraction of around 18 %.
Concerning the homogenized stiffness tensor components, we remark that the optimization procedure reduces the volume fraction at the expense of the stiffness, when dealing with small ranges of admissible values.

To summarize, all the preliminary considerations above have to be taken into account in a realistic modeling of new stents in order to match the recommended pre-clinical assessment targets.

4.3 New stent designs: structural mechanics and CFD analysis

The FE analysis suggests that only Designs 1 and 5 meet the minimum requirements for usability throughout the implantation procedure, in terms of device crimpability into the catheter. When compared to Design 5, Design 1 exhibits: a lower value of the peak maximum principal strain at the catheter diameter, i.e., a higher safety in terms of structural integrity, with reference to the material elongation at break limit; a higher radial force; a similar foreshortening at the implantation diameter (see Table 4).

More in detail, despite the regulatory documentation [34, 33] does not enforce limit values, the radial force should not be too low, to avoid incomplete apposition of the stent to the vessel wall, nor excessive, to limit injuring of the surrounding tissue; the foreshortening should be ideally as close as possible to zero, to precisely implant the device into the vessel [3]. In [78], the authors experimentally evaluated the radial force generated by three commercially available self-expandable peripheral stents, when considering a radial compression of 1 mm in diameter, establishing that such a force is expected to be in the range [0.4 N/mm, 1 N/mm]. The radial force

of Designs 1 and 5, at the same diameter of radial compression, are equal to 0.65 N/mm and 0.17 N/mm, respectively (Table 4). Accordingly, the radial force generated by Design 1 is within the reference range, whereas Design 5 features a force value out of the range.

With reference to hemodynamics, Design 1, which is characterized by a slightly higher volume fraction, exhibits lower TAWSS and higher TSVI median values than Design 5 (Fig. 9). It follows that Design 1 may be subject to a higher risk of ISR [72, 31, 79, 80].

Summarizing, the findings of the structural mechanics and fluid dynamics analyses suggest that Design 1 is better in terms of mechanical characteristics (i.e., lower peak maximum principal strain, radial force in the range of commercial devices), while Design 5 is better in terms of geometric (i.e., lower contact area) and hemodynamics characteristics. Further investigation is required to define the best stent design, through the execution of other *in silico* tests (e.g., crush and kink tests) and the fabrication of real prototypes for a final *in vitro* assessment.

4.4 Current limits and future perspectives

The proposed workflow proved to be a reliable computational tool to generate innovative stent designs that ensure adequate performances in terms of usability, radial force and hemodynamics. However, the actual effectiveness of the procedure might suffer from some restrictions. For instance, the investigation carried out in Section 3 is confined to specific choices for the selected components of the homogenized stiffness tensor as well as for the associated range of variation. In addition, the mechanical performance of the stents has been assessed by simulating the radial crimping only, whereas *in vivo* conditions in femoropopliteal arteries imply more complex loading conditions related to the lower limb movements [28, 29]. Finally, although laser cutting manufacturing is flexible enough to generate complex stent geometries starting from computer aided design data, at the moment, the proposed framework does not include any manufacturing constraints and no prototypes of the obtained designs have been tested for realization.

Several advances could be implemented to further extend the potentiality of the presented workflow. As a possible, although very challenging, enhancement, we plan to include the requirements – currently employed to a posteriori assess the biomechanical behavior of new stent devices – into the optimization problem (11), for instance as additional constraints or by modifying the goal functional. Moreover, a multiphysics TO-based approach could be developed thus enriching the structural mechanics requirements addressed in this paper with manufacturability constraints in the design of 2D stent unit cells. In addition, the proposed computational workflow could be further improved by optimizing the choice of the selected NiTi alloy, in order to take into account the dependence of the NiTi material properties

on the chemical composition and on the thermo-mechanical processing operations [81]. Finally, thanks to high flexibility of the proposed pipeline, it could be interesting to apply it to the improvement/design of medical devices for other cardiovascular applications or for different medical areas (we refer to [44] for an instance of orthopedic application).

5 Conclusions

In the last decade the technological innovation in femoral artery stenting has been incremental, with minimal modifications to the geometry of consolidated stent designs, resulting in marginal improvements in stents performance. Such an incremental approach considerably limits the proposal of innovative devices on the market. On the contrary, the proposed computational workflow enables the creation of breakthrough designs of self-expandable femoral artery stents, thanks to the employment of inverse homogenization TO for the generation of new stent unit cells that meet specific clinical requirements. Five proof-of-concept stent designs with different topologies were successfully generated and *in silico* verifications were carried out to assess the associated mechanical and hemodynamic performance. Two of the identified stent designs exhibited promising results in terms of stent usability throughout the implantation procedure, low values for the surface contact area and adequate radial force.

Overall, the method has to be meant as a proof-of-concept to assess the capability of the workflow in Fig. 1 to match a set of specific requirements for the stent design. The versatility of the involved methodology guarantees the generalization of the whole process to different objectives, up to a patient-specific setting.

Acknowledgements

NF and SP thank the PRIN research grant n.20204LN5N5 *Advanced Polyhedral Discretisations of Heterogeneous PDEs for Multiphysics Problems*. NF acknowledges the INdAM–GNCS 2023 Project *Algoritmi efficienti per la gestione e adattazione di mesh poligonali*. CC, DG and UM acknowledge the Italian Ministry of Education, University and Research for the research grant FISR2019 03221 *CECOMES*. ALA, CC and DC acknowledge the Piedmont Region, Italy for the research grant POR FESR PiTeF 2014-20 351-96 *Nitiliera*.

References

[1] M. Hejazi, F. Sassani, J. Gagnon, Y. Hsiang, A. S. Phani, Deformation mechanics of self-expanding venous stents: Modelling and experiments,

J. Biomech. 120 (2021) 110333. arXiv:2102.10219, doi:10.1016/j.jbiomech.2021.110333.

[2] W. Jiang, W. Zhao, T. Zhou, L. Wang, T. Qiu, A Review on manufacturing and post-processing technology of vascular stents, Micromachines 13 (1) (2022) 140. doi:10.3390/mi13010140.

[3] C. Pan, Y. Han, J. Lu, Structural design of vascular stents: A review, Micromachines 12 (7) (2021) 770. doi:10.3390/mi12070770.

[4] B. Polanec, J. Kramberger, S. Glodež, A review of production technologies and materials for manufacturing of cardiovascular stents, Adv. Prod. Eng. Manag. 15 (4) (2020) 390–402. doi:10.14743/APEM2020.4.373.

[5] T. Duerig, M. Wholey, A comparison of balloon- and self-expanding stents, Minim. Invasive Ther. Allied Technol. 11 (4) (2002) 173–178. doi:doi:10.1080/136457002760273386.

[6] T. Schmidt, J. D. Abbott, Coronary stents: History, design, and construction, J. Clin. Med. 7 (6) (2018) 126. doi:10.3390/jcm7060126.

[7] W. Kim, D. Choi, Treatment of femoropopliteal artery in-stent restenosis, Korean Circ. J. 48 (3) (2018) 191–197. doi:10.4070/kcj.2018.0074.

[8] E. Shlofmitz, M. Iantorno, R. Waksman, Restenosis of drug-eluting stents: A new classification system based on disease mechanism to guide treatment and state-of-the-art review, Circ. Cardiovasc. Interv. 12 (8) (2019) e007023. doi:10.1161/CIRCINTERVENTIONS.118.007023.

[9] B. Tomberli, A. Mattesini, G. I. Baldereschi, C. Di Mario, A Brief history of coronary artery stents, Revista Espanola de Cardiologia 71 (5) (2018) 312–319. doi:10.1016/j.recesp.2017.11.016.

[10] A. K. Kareem, M. M. Gabir, I. R. Ali, A. E. Ismail, I. Taib, N. Darlis, O. M. Almoayed, A review on femoropopliteal arterial deformation during daily lives and nickel-titanium stent properties, J. Med. Eng. Technol. 46 (4) (2022) 300–317. doi:10.1080/03091902.2022.2041749.

[11] A. Qiao, Z. Zhang, Numerical simulation of vertebral artery stenosis treated with different stents, J. Biomech. Eng. 136 (4) (2014) 041007. doi:10.1115/1.4026229.

[12] R. A. Byrne, M. Joner, A. Kastrati, Stent thrombosis and restenosis: What have we learned and where are we going? the Andreas Grüntzig Lecture ESC 2014, Eur. Heart J. 36 (47) (2015) 3320–3331. doi:10.1093/eurheartj/ehv511.

[13] R. Reejhsinghani, A. S. Lotfi, Prevention of stent thrombosis: Challenges and solutions, Vasc. Health Risk Manag. 11 (2015) 93–106. doi:10.2147/VHRM.S43357.

[14] T. M. Morrison, M. L. Dreher, S. Nagaraja, L. M. Angelone, W. Kainz, The role of computational modeling and simulation in the total product life cycle of peripheral vascular devices, J. Med. Devices 11 (2) (2017) 024503. doi:10.1115/1.4035866.

[15] T. M. Morrison, P. Pathmanathan, M. Adwan, E. Margerrison, Advancing regulatory science with computational modeling for medical devices at the FDA's office of science and engineering laboratories, Front. Med. 5 (2018) 241. doi:10.3389/fmed.2018.00241.

[16] G. Alaimo, F. Auricchio, M. Conti, M. Zingales, Multi-objective optimization of nitinol stent design, Med. Eng. Phys. 47 (2017) 13–24. doi:10.1016/j.medengphy.2017.06.026.

[17] R. Clune, D. Kelliher, J. C. Robinson, J. S. Campbell, NURBS modeling and structural shape optimization of cardiovascular stents, Struct. Multidiscip. Optim. 50 (1) (2014) 159–168. doi:10.1007/s00158-013-1038-y.

[18] E. Masoumi Khalil Abad, D. Pasini, R. Cecere, Shape optimization of stress concentration-free lattice for self-expandable Nitinol stent-grafts, J. Biomech. 45 (6) (2012) 1028–1035. doi:10.1016/j.jbiomech.2012.01.002.

[19] S. Pant, G. Limbert, N. P. Curzen, N. W. Bressloff, Multiobjective design optimisation of coronary stents, Biomaterials 32 (31) (2011) 7755–7773. doi:10.1016/j.biomaterials.2011.07.059.

[20] S. Pant, N. W. Bressloff, G. Limbert, Geometry parameterization and multidisciplinary constrained optimization of coronary stents, Biomech. Model. Mechanobiol. 11 (1-2) (2012) 61–82. doi:10.1007/s10237-011-0293-3.

[21] N. S. Ribeiro, J. Folgado, H. C. Rodrigues, Surrogate-based multiobjective design optimization of a coronary stent: Altering geometry toward improved biomechanical performance, nt. J. for Numer. Methods Biomed. Eng. 37 (6) (2021) e3453. doi:10.1002/cnm.3453.

[22] W. Wu, L. Petrini, D. Gastaldi, T. Villa, M. Vedani, E. Lesma, B. Previtali, F. Migliavacca, Finite element shape optimization for biodegradable magnesium alloy stents, Ann. Biomed. Eng. 38 (9) (2010) 2829–2840. doi:10.1007/s10439-010-0057-8.

[23] M. P. Bendsoe, O. Sigmund, Topology Optimization: Theory, Methods and Applications, 2nd Edition, Springer, 2004.

[24] W. Wu, D. Z. Yang, Y. Y. Huang, M. Qi, W. Q. Wang, Topology optimization of a novel stent platform with drug reservoirs, Med. Eng. Phys. 30 (9) (2008) 1177–1185. doi:10.1016/j.medengphy.2008.02.010.

[25] K. A. James, H. Waisman, Layout design of a bi-stable cardiovascular stent using topology optimization, Comput. Methods Appl. Mech. Engrg. 305 (2016) 869–890. doi:10.1016/j.cma.2016.02.036.

[26] H. Xue, Z. Luo, T. Brown, S. Beier, Design of self-expanding auxetic stents using topology optimization, Front. Bioeng. Biotechnol. 8 (2020) 736. doi:10.3389/fbioe.2020.00736.

[27] H. Xue, S. C. Saha, S. Beier, N. Jepson, Z. Luo, Topological optimization of auxetic coronary stents considering hemodynamics, Front. Bioeng. Biotechnol. 9 (2021) 728914. doi:10.3389/fbioe.2021.728914.

[28] C. P. Cheng, N. M. Wilson, R. L. Hallett, R. J. Herfkens, C. A. Taylor, In vivo MR angiographic quantification of axial and twisting deformations of the superficial femoral artery resulting from maximum hip and knee flexion, J. Vasc. Interv. Radiol. 17 (6) (2006) 979–987. doi:10.1097/01.RVI.0000220367.62137.e8.

[29] J. N. MacTaggart, N. Y. Phillips, C. S. Lomneth, I. I. Pipinos, R. Bowen, B. Timothy Baxter, J. Johanning, G. Matthew Longo, A. S. Desyatova, M. J. Moulton, Y. A. Dzenis, A. V. Kamenskiy, Three-dimensional bending, torsion and axial compression of the femoropopliteal artery during limb flexion, J. Biomech. 47 (10) (2014) 2249–2256. doi:10.1016/j.jbiomech.2014.04.053.

[30] N. Ferro, S. Micheletti, S. Perotto, Density-based inverse homogenization with anisotropically adapted elements, in: A. Corsini, S. Perotto, G. Rozza, H. van Brummelen (Eds.), Numerical Methods for Flows, vol 132. Lecture Notes in Computational Science and Engineering., Springer, 2020, pp. 211–221. doi:https://doi.org/10.1007/978-3-030-30705-9_19.

[31] K. C. Koskinas, Y. S. Chatzizisis, A. P. Antoniadis, G. D. Giannoglou, Role of endothelial shear stress in stent restenosis and thrombosis: Pathophysiologic mechanisms and implications for clinical translation, J. Am. College Cardiol. 59 (15) (2012) 1337–1349. doi:10.1016/j.jacc.2011.10.903.

[32] D. Károly, M. Kovács, A. A. Terdik, E. Bognár, Investigation of metallic surface area of coronary stents, Biomechanica Hungarica 6. doi:10.17489/biohun/2013/1/23.

[33] ISO, Cardiovascular implants — Endovascular devices — Part 2: Vascular stents (2012).

[34] FDA, Non-clinical engineering tests and recommended labeling for intravascular stents and associated delivery systems (2010).

[35] A. Bensoussan, J. L. Lions, G. Papanicolaou, Asymptotic Analysis for Periodic Structures, AMS Chelsea Publishing, Providence, RI, 2011.

[36] O. Sigmund, Design of material structures using topology optimization, Ph.D. thesis, Technical University of Denmark, Lyngby, Denmark (1994).

[37] P. Helnwein, Some remarks on the compressed matrix representation of symmetric second-order and fourth-order tensors, Comput. Methods Appl. Mech. Engrg. 190 (22-23) (2001) 2753–2770. doi:https://doi.org/10.1016/S0045-7825(00)00263-2.

[38] A. Ern, J.-L. Guermond, Theory and practice of finite elements, Vol. 159 of Applied Mathematical Sciences, Springer-Verlag, New York, 2004.

[39] O. Sigmund, J. Petersson, Numerical instabilities in topology optimization: a survey on procedures dealing with checkerboards, mesh-dependencies and local minima, Struct. Optim. 16 (1) (1998) 68–75. doi:https://doi.org/10.1007/BF01214002.

[40] S. Micheletti, S. Perotto, L. Soli, Topology optimization driven by anisotropic mesh adaptation: towards a free-form design, Comput. Struct. 214 (2019) 60 – 72. doi:https://doi.org/10.1016/j.compstruc.2019.01.005.

[41] N. Ferro, S. Micheletti, S. Perotto, POD-assisted strategies for structural topology optimization, Comput. Math. Appl. 77 (10) (2019) 2804–2820. doi:https://doi.org/10.1016/j.camwa.2019.01.010.

[42] N. Ferro, S. Micheletti, S. Perotto, Compliance–stress constrained mass minimization for topology optimization on anisotropic meshes, SN Appl. Sci. 2 (7) (2020) 1–11. doi:https://doi.org/10.1007/s42452-020-2947-1.

[43] D. di Cristofaro, C. Galimberti, D. Bianchi, R. Ferrante, N. Ferro, M. Mannisi, S. Perotto, Adaptive topology optimization for innovative 3D printed metamaterials, in: Proceedings of WCCM-ECCOMAS

2020 Conference - Modeling and Analysis of Real World and Industry Applications, Vol. 1200, 2021.

[44] N. Ferro, S. Perotto, D. Bianchi, R. Ferrante, M. Mannisi, Design of cellular materials for multiscale topology optimization: application to patient-specific orthopedic devices, Struct. Multidiscip. Optim. 65 (3) (2022) 79. doi:https://doi.org/10.1007/s00158-021-03163-z.

[45] N. Ferro, S. Perotto, M. Gavazzoni, A new fluid-based strategy for the connection of non-matching lattice materials, Struct. Multidiscip. Optim. 65 (10) (2022) Paper No. 287, 15. doi:https://doi.org/10.1007/s00158-022-03354-2.

[46] K. E. Jensen, Solving stress and compliance constrained volume minimization using anisotropic mesh adaptation, the method of moving asymptotes and a global p-norm, Struct. Multidiscip. Optim. 54 (4) (2016) 831–841. doi:https://doi.org/10.1007/s00158-016-1439-9.

[47] O. C. Zienkiewicz, J. Z. Zhu, A simple error estimator and adaptive procedure for practical engineering analysis, Int. J. Numer. Methods Eng. 24 (2) (1987) 337–357. doi:https://doi.org/10.1002/nme.1620240206.

[48] O. C. Zienkiewicz, J. Z. Zhu, The superconvergent patch recovery and a posteriori error estimates. Part I. The recovery technique, Int. J. Numer. Methods Eng. 33 (7) (1992) 1331–1364. doi:https://doi.org/10.1002/nme.1620330702.

[49] R. Rodríguez, Some remarks on Zienkiewicz-Zhu estimator, Numer. Methods Partial Differential Equations 10 (5) (1994) 625–635. doi:https://doi.org/10.1002/num.1690100509.

[50] C. Carstensen, All first-order averaging techniques for a posteriori finite element error control on unstructured grids are efficient and reliable, Math. Comp. 73 (247) (2004) 1153–1165.

[51] A. Naga, Z. Zhang, A posteriori error estimates based on the polynomial preserving recovery, SIAM J. Numer. Anal. 42 (4) (2004) 1780–1800. doi:https://doi.org/10.1137/S0036142903413002.

[52] N. Yan, A. Zhou, Gradient recovery type a posteriori error estimates for finite element approximations on irregular meshes, Comput. Methods Appl. Mech. Engrg. 190 (32-33) (2001) 4289–4299. doi:https://doi.org/10.1016/S0045-7825(00)00319-4.

[53] G. Maisano, S. Micheletti, S. Perotto, C. L. Bottasso, On some new recovery-based a posteriori error estimators, Comput. Methods Appl. Mech. Engrg. 195 (37-40) (2006) 4794–4815. doi:https://doi.org/10.1016/j.cma.2005.07.024.

[54] S. Micheletti, S. Perotto, Anisotropic adaptation via a Zienkiewicz-Zhu error estimator for 2D elliptic problems, in: G. Kreiss, P. Lötstedt, A. Målqvist, M. Neytcheva (Eds.), Numerical Mathematics and Advanced Applications, Springer-Verlag Berlin Heidelberg, 2010, pp. 645–653. doi:https://doi.org/10.1007/978-3-642-11795-4_69.

[55] S. Micheletti, S. Perotto, Reliability and efficiency of an anisotropic Zienkiewicz-Zhu error estimator, Comput. Methods Appl. Mech. Engrg. 195 (9-12) (2006) 799–835. doi:https://doi.org/10.1016/j.cma.2005.02.009.

[56] F. Hecht, New development in FreeFem++, J. Numer. Math. 20 (3-4) (2012) 251–265. doi:https://doi.org/10.1515/jnum-2012-0013.

[57] A. Wächter, L. T. Biegler, On the implementation of an interior-point filter line-search algorithm for large-scale nonlinear programming, Math. Program. 1, Ser. A (106) (2006) 25–57. doi:https://doi.org/10.1007/s10107-004-0559-y.

[58] F. Hecht, BAMG: Bidimensional anisotropic mesh generator, https://www.ljll.math.upmc.fr/hecht/ftp/bamg/bamg.pdf (2006).

[59] S.-W. Cheng, T. K. Dey, J. R. Shewchuk, Delaunay mesh generation, Chapman & Hall/CRC Computer and Information Science Series, Chapman & Hall/CRC, Boca Raton, FL, 2013.

[60] N. Ferro, S. Micheletti, S. Perotto, An optimization algorithm for automatic structural design, Comput. Methods Appl. Mech. Engrg. 372 (2020) 113335. doi:https://doi.org/10.1016/j.cma.2020.113335.

[61] S. Xu, Y. Cai, G. Cheng, Volume preserving nonlinear density filter based on heaviside functions, Struct. Multidisc. Optim. 41 (2010) 495–505. doi:https://doi.org/10.1007/s00158-009-0452-7.

[62] F. Wang, B. S. Lazarov, O. Sigmund, On projection methods, convergence and robust formulations in topology optimization, Struct. Multidisc. Optim. 43 (2011) 767–784. doi:https://doi.org/10.1007/s00158-010-0602-y.

[63] M. Gavazzoni, N. Ferro, S. Perotto, S. Foletti, Multi-physics inverse homogenization for the design of innovative cellular materials: Application to thermo-elastic problems, Math. Comput. Appl. 27 (1) (2022) 15. doi:https://doi.org/10.3390/mca27010015.

[64] M. Colombo, A. Corti, D. Gallo, A. Colombo, G. Antognoli, M. Bernini, C. McKenna, S. Berceli, T. Vaughan, F. Migliavacca, C. Chiastra, Superficial femoral artery stenting: Impact of stent design and overlapping on the local hemodynamics, Comput. Biol. Med. 144 (2022) 105248. doi:10.1016/j.compbiomed.2022.105248.

[65] C. Capelli, F. Gervaso, L. Petrini, G. Dubini, F. Migliavacca, Assessment of tissue prolapse after balloon-expandable stenting: Influence of stent cell geometry, Med. Eng. Phys. 31 (4) (2009) 441–447. doi:10.1016/j.medengphy.2008.11.002.

[66] C. Chiastra, M. J. Grundeken, C. Collet, W. Wu, J. J. Wykrzykowska, G. Pennati, G. Dubini, F. Migliavacca, Biomechanical impact of wrong positioning of a dedicated stent for coronary bifurcations: A virtual bench testing study, Cardiovasc. Eng. Technol. 9 (3) (2018) 415–426. doi:10.1007/s13239-018-0359-9.

[67] F. Auricchio, R. L. Taylor, J. Lubliner, Shape-memory alloys: Macromodelling and numerical simulations of the superelastic behavior, Comput. Methods Appl. Mech. Engrg. 146 (3-4) (1997) 281–312. doi:10.1016/S0045-7825(96)01232-7.

[68] A. Finotello, R. Gorla, N. Brambilla, F. Bedogni, F. Auricchio, S. Morganti, Finite element analysis of transcatheter aortic valve implantation: Insights on the modelling of self-expandable devices, J. Mech. Behavior Biomed. Mater. 123 (June) (2021) 104772. doi:10.1016/j.jmbbm.2021.104772.

[69] D. Carbonaro, C. Chiastra, U. Morbiducci, A. Audenino, Transcatheter aortic valve with embolic filter: Experiments and simulations, in: Convegno Nazionale di Bioingegneria, 2020, pp. 457–460.

[70] D. Carbonaro, D. Gallo, U. Morbiducci, A. Audenino, C. Chiastra, In silico biomechanical design of the metal frame of transcatheter aortic valves: multi-objective shape and cross-sectional size optimization, Struct. Multidiscip. Optim. 64 (4) (2021) 1825–1842. doi:10.1007/s00158-021-02944-w.

[71] L. Petrini, E. Dordoni, D. Allegretti, D. Pott, M. Kütting, F. Migliavacca, G. Pennati, Simplified multistage computational approach to assess the fatigue behavior of a niti transcatheter aortic valve during in vitro tests: A proof-of-concept study, J. Med. Devices 11 (2) (2017) 021009. doi:10.1115/1.4035791.

[72] C. Chiastra, V. Mazzi, M. Lodi Rizzini, K. Calò, A. Corti, A. Acquasanta, G. De Nisco, D. Belliggiano, E. Cerrato, D. Gallo, U. Morbiducci,

Coronary artery stenting affects wall shear stress topological skeleton, J. Biomech. Eng. 144 (6) (2022) 1–11. doi:10.1115/1.4053503.

[73] C. Chiastra, D. Gallo, P. Tasso, F. Iannaccone, F. Migliavacca, J. J. Wentzel, U. Morbiducci, Healthy and diseased coronary bifurcation geometries influence near-wall and intravascular flow: A computational exploration of the hemodynamic risk, J. Biomech. 58 (2017) 79–88. doi:10.1016/j.jbiomech.2017.04.016.

[74] V. Mazzi, G. De Nisco, A. Hoogendoorn, K. Calò, C. Chiastra, D. Gallo, D. A. Steinman, J. J. Wentzel, U. Morbiducci, Early atherosclerotic changes in coronary arteries are associated with endothelium shear stress contraction/expansion variability, Ann. Biomed. Eng. 49 (9) (2021) 2606–2621. doi:10.1007/s10439-021-02829-5.

[75] V. Mazzi, U. Morbiducci, K. Calò, G. De Nisco, M. L. Rizzini, E. Torta, G. C. A. Caridi, C. Chiastra, D. Gallo, Wall shear stress topological skeleton analysis in cardiovascular flows: Methods and applications, Mathematics 9 (7) (2021) 720. doi:10.3390/math9070720.

[76] G. De Nisco, P. Tasso, K. Calò, V. Mazzi, D. Gallo, F. Condemi, S. Farzaneh, S. Avril, U. Morbiducci, Deciphering ascending thoracic aortic aneurysm hemodynamics in relation to biomechanical properties, Med. Eng. Phys. 82 (2020) 119–129. doi:10.1016/j.medengphy.2020.07.003.

[77] U. Morbiducci, V. Mazzi, M. Domanin, G. De Nisco, C. Vergara, D. A. Steinman, D. Gallo, Wall shear stress topological skeleton independently predicts long-term restenosis after carotid bifurcation endarterectomy, Ann. Biomed. Eng. 48 (12) (2020) 2936–2949. doi:10.1007/s10439-020-02607-9.

[78] T. Matsumoto, Y. Matsubara, Y. Aoyagi, D. Matsuda, J. Okadome, K. Morisaki, K. Inoue, S. Tanaka, T. Ohkusa, Y. Maehara, Radial force measurement of endovascular stents: Influence of stent design and diameter, Vascular 24 (2) (2016) 171–176. doi:10.1177/1708538115590040.

[79] M. Colombo, Y. He, A. Corti, D. Gallo, F. Ninno, S. Casarin, J. M. Rozowsky, F. Migliavacca, S. Berceli, C. Chiastra, In-stent restenosis progression in human superficial femoral arteries: dynamics of lumen remodeling and impact of local hemodynamics, Ann. Biomed. Eng. 49 (9) (2021) 2349–2364. doi:10.1007/s10439-021-02776-1.

[80] M. Colombo, Y. He, A. Corti, D. Gallo, S. Casarin, J. M. Rozowsky, F. Migliavacca, S. Berceli, C. Chiastra, Baseline local hemodynamics as predictor of lumen remodeling at 1-year follow-up in stented

superficial femoral arteries, Sci. Reports 11 (1) (2021) 1613. doi:10.1038/s41598-020-80681-8.

[81] D. Carbonaro, S. Zambon, A. Corti, D. Gallo, U. Morbiducci, L. Audenino, C. Chiastra, Impact of nickel – titanium super-elastic material properties on the mechanical performance of self-expandable transcatheter aortic valves, J. Mech. Behavior Biomed. Mater. 138 (2023) 105623. doi:10.1016/j.jmbbm.2022.105623.

MOX Technical Reports, last issues

Dipartimento di Matematica
Politecnico di Milano, Via Bonardi 9 - 20133 Milano (Italy)

28/2023 Zingaro, A.; Vergara, C.; Dede', L.; Regazzoni, F.; Quarteroni, A.
A comprehensive mathematical model for myocardial perfusion

27/2023 Beirao da Vega, L.; Canuto, C.; Nochetto, R.H.; Vacca, G.; Verani, M.
Adaptive VEM for variable data: convergence and optimality

Fumagalli, A.; Panzeri, L.; Formaggia, L.; Scotti, A.; Arosio, D.
A mixed-dimensional model for direct current simulations in presence of a thin high-resistivity liner

26/2023 Artoni, A.; Antonietti, P.F.; Corradi, R.; Mazzieri, I.; Parolini, N.; Rocchi, D.; Schito P.; Semeraro, F.F.;
AeroSPEED: a high order acoustic solver for aeroacoustic applications

25/2023 Bonetti, S.; Botti, M.; Mazzieri, I.; Antonietti, P.F.
Numerical modelling of wave propagation phenomena in thermo-poroelastic media via discontinuous Galerkin methods

24/2023 Costa, G.; Cavinato, L.; Fiz, F.; Sollini, M.; Chiti, A.; Torzilli, G.; Ieva, F.; Viganò, L.
Mapping Tumor Heterogeneity via Local Entropy Assessment: Making Biomarkers Visible

23/2023 Bertoletti, A.; Cannistrà, M.; Diaz Lema, M.; Masci, C.; Mergoni, A.; Rossi, L.; Soncin, M.
The Determinants of Mathematics Achievement: A Gender Perspective Using Multilevel Random Forest

22/2023 Su, Y.; Riccobelli, D.; Chen, Y; Chen, W; Ciarletta, P
Designing dielectric-elastomer balloons with tunable shapes in response to electro-mechanical stimuli

21/2023 Cavinato, L.; Sollini, M.; Ragni, A.; Bartoli, F.; Zanca, R.; Pasqualetti, F.; Marciano, A.; Ieva, F.; and Erba, A.P.
Radiomics-based Inter-lesion Relation Network to Describe [18F]FMCH PET/CT Imaging Phenotypes in Prostate Cancer

17/2023 Savin, M.S.; Cavinato, L.; Costa, G.; Fiz, F.; Torzilli, G.; Vigano', L.; Ieva, F.
Distant supervision for imaging-based cancer sub-typing in Intrahepatic Cholangiocarcinoma